2012

System Optimization and Patient Translational Motion Correction for Reduction of Artifacts in a Fan-Beam CT Scanner

Zachary Gordon Lee Wise
Wright State University

System Optimization and Patient Translational Motion Correction for Reduction of Artifacts in a Fan-Beam CT Scanner

A thesis submitted in partial fulfillment
of the requirements for the degree of
Master of Science in Engineering

By

Zachary Gordon Lee Wise
B.S., Wright State University, 2009

2012
Wright State University

WRIGHT STATE UNIVERSITY
SCHOOL OF GRADUATE STUDIES

August 2, 2012

I HEREBY RECOMMEND THAT THE THESIS PREPARED UNDER MY SUPERVISION BY Zachary Gordon Lee Wise ENTITLED System Optimization and Patient Translational Motion Correction for Reduction of Artifacts in a Fan-Beam CT Scanner BE ACCEPTED IN PARTIAL FULFILLMENT OF THE REQUIREMENTS FOR THE DEGREE OF Master of Science in Engineering.

Thomas N. Hangartner, Ph.D.
Thesis Director

Thomas N. Hangartner, Ph.D.
Chair, Department of Biomedical,
Industrial and Human Factors Engineering

Committee on
Final Examination

Thomas N. Hangartner, Ph.D.

Julie A. Skipper, Ph.D.

David F. Short, M.S.

Andrew Hsu, Ph.D.
Dean, Graduate School

Abstract

Wise, Zachary Gordon Lee, M.S.Egr., Department of Biomedical, Industrial and Human Factors Engineering, Wright State University, Dayton, OH, 2012. **System Optimization and Patient Translational Motion Correction for Reduction of Artifacts in a Fan-Beam CT Scanner.**

In computed tomography (CT) systems, many different artifacts may be present in the reconstructed image. These artifacts can greatly reduce image quality. For our laboratory prototype CT system, a fan-beam/cone-beam focal high-resolution computed tomography (fHRCT) scanner, the major artifacts that affect image quality are distortions due to errors in the reconstruction algorithm's geometric parameters, ring artifacts caused by uncalibrated detectors, cupping and streaking created by beam hardening, and patient-based motion artifacts. Optimization of the system was required to reduce the effects of the first three artifact types, and an algorithm for correction of translational motion was developed for the last.

System optimization of the system occurred in three parts. First, a multi-step process was developed to determine the geometric parameters of the scanner. The ability of the source-detector gantry to translate allowed a precise method to be created for calculating these parameters. Second, a general flat-field correction was used to linearize the detectors and reduce the ring artifacts. Lastly, beam hardening artifacts were decreased

by a preprocessing technique. This technique assumes linear proportionality between the thickness of the calibration material, aluminum, and the experimental measurement of $ln(N_o/N)$, where N_o is the total number of photons entering the material and N is the number of photons exiting the material.

In addition to system optimization to minimize artifacts, an algorithm for correction of translational motion was developed and implemented. In this method, the integral mass and center of mass at each projection angle was seen to follow a sinusoidal or sinusoidal-like curve. Fits were used on the motion-encoded sinograms to determine both of these curves and, consequently, the amount and direction of motion that occurred. Each projection was individually adjusted to compensate for this motion by widening or narrowing the projection based on the ratio of the actual and calculated ideal projection integrals and shifting the projection to match the actual centroid to the calculated ideal location.

A custom imaging phantom with an outer diameter of approximately 16 mm was used to test the motion-correction algorithm in both simulated and experimental cases. A baseline of the error measured, taken as a fraction, was established as 0.16 for motion-free images measured on the scanner. Various motion patterns were tested. These included the distance of motion, the angle at which the motion occurred, and the ratio of the sinograms that was corrupted by motion. Experimental testing showed a maximum error increase of 2.7% from the baseline error for the motion-corrected images at 4 mm motion.

The overall optimization provided acceptable results for the reconstructed image and good-quality projections for use in the motion-correction algorithm. Distortion and ring

artifacts were almost completely removed, and the beam hardening artifacts were greatly reduced. The motion-correction algorithm implemented in this thesis helps minimize the amount of error due to translational motion and provides a foundation for future corrections of more complex motions.

Table of Contents

1. Introduction 1

1.1 Description of the System 1

1.2 Scanner Optimization 2

1.3 Patient Motion Correction 2

2. Optimization of System for Reduction of Scanner Artifacts 3

2.1 Parameter Calculation 3

2.1.1 Method for Parameters Calculation 5

2.1.2 Parameter Calculation Results 17

2.2 Detector Linearization 20

2.2.1 Method for Detector Linearization 21

2.2.2 Detector Linearization Results 24

2.3 Beam Hardening 25

2.3.1 Method for Beam Hardening Correction 25

2.3.2 Beam Hardening Correction Results 27

2.4 Reconstruction and Results 28

3. Correction for Patient Translational Motion 31

3.1 Methods for Translational Motion Correction 35

3.1.1 Determination of Ideal Data for the Definite Integral and the Center of Mass of the Sinogram. 35

3.1.2 Correction of Sinogram Image 39

3.2 Method for Determining Error between Motion-Free and Motion-Corrected Images 40

3.3 Results 42

3.3.1 Qualitative Analysis 42

3.3.2 Quantitative Analysis 54

4. Conclusion 60

4.1 Scanner Optimization 60

4.2 Patient Motion Correction 62

5. References 67

Table of Figures

Figure 2-1. Fan-beam geometry with a midline offset from the center-of-rotation at gantry angle β. (adapted from [1]) 4

Figure 2-2. Centroid of the pin for two full third-generation scans. Centroid A and Centroid B show the centroid of a pin located at (x_o, y_o) at differing midline offset values τ. E for this example is detector element 0. 6

Figure 2-3. The difference of the rays incident on the pin from the two translation positions. (a) shows the difference as d_1 given the gantry angle at arbitrary position β_i and (b) shows the difference as d_2 given the complementary gantry angle of $\beta_i, \beta_i+\pi$. The midlines of the sources are not perpendicular to the line that traverses the center-of-rotation and the pin. Therefore $d_1 \neq d_2$. The detector is assumed to be fixed for simplicity. 7

Figure 2-4. The difference of the rays incident on the pin from the two translation positions. (a) shows the difference as d_1 given the special gantry angle of β_{normal} and (b) shows the difference as d_2 given the complementary gantry angle of $\beta_{normal}, \beta_{normal}+\pi$. The midlines of the sources are now perpendicular to the line that traverses the center-of-rotation and the pin. Therefore $d_1 = d_2$. Again, the detector is assumed to be fixed for simplicity. 8

Figure 2-5. Difference between Centroid A and Centroid B at all projection angles..... 9

Figure 2-6. Absolute difference of $\Delta AB(\beta)$ and $\Delta AB(\beta+\pi)$ for $0 \leq \beta < \pi$. 10

Figure 2-7. The translation scan taken at (a) $\beta_{normal} + \pi/2$ and (b) $\beta_{normal} - \pi/2$, where the midline for each is paralle1 to the line that traverses the center-of-rotation and the pin. 11

Figure 2-8. The projection of the pin vs. translation position of the source for the translational scan at $\beta_{normal} + \pi/2$(Translation Scan 1) and $\beta_{normal} - \pi/2$(Translation Scan 2). 11

Figure 2-9. The translation scan taken at (a) β_{normal} and (b) $\beta_{normal} + \pi$, where the midline for each is perpendicular to the line that traverses the center-of-rotation and the pin. 12

Figure 2-10. The translation position of the source vs. projection of the pin for the translational scan at β_{normal} and $\beta_{normal} + \pi$. In this instance the Euclidean distance is 6 units and, consequently, the pin is 3 units from the center. 13

Figure 2-11. Linear region of Figure 2-8 showing the projection of the pin vs. the translation position of the source for the translational scan at $\beta_{normal} + \pi/2$ and $\beta_{normal} - \pi/2$. 14

Figure 2-12. The geometric relationships used to determine the parameters *D* and *Rd* where (a) shows the position of the pin at $\beta_{normal} + \pi/2$, (b) shows the position of the pin at $\beta_{normal} - \pi/2$, (c) shows the effect of a translation of the source on the projection of the pin on the detector given the source at $\beta_{normal} + \pi/2$, and (d) shows the effect of a translation of the source on the projection of the pin on the detector given the source at $\beta_{normal} - \pi/2$. 15

Figure 2-13. Centroid of the pin for two full third-generation scans. Centroid A and Centroid B show the centroid at differing midline offset values τ. 17

Figure 2-14. Difference between Centroid A and Centroid B at all projection angles.... 18

Figure 2-15. Absolute difference of $\Delta AB(\beta)$ and $\Delta AB(\beta+\pi)$ for $0 \leq \beta < \pi$. 19

Figure 2-16. Linear region of the projection of the pin vs. the translation position of the source for the translational scan at $\beta_{normal} + \pi/2$ (data1) and $\beta_{normal} - \pi/2$ (data2). 20

Figure 2-17. Graph showing the actual and ideal response of a representative detector element. 22

Figure 2-18. Two images of the same open field projection shown as (top) the raw data image and (bottom) the image of the linearized data. The bright spot in the linearized data indicates a collection of dead pixels in the detector. 24

Figure 2-19. Graph of the actual and ideal response of the detector with increasing thickness of aluminum in the source-to-detector path. 26

Figure 2-20. Graph of the linearized data before and after correction for beam hardening. 28

2-21. Reconstruction of the image before geometric optimization, detector linearization, or beam hardening correction. 29

Figure 2-22. Reconstruction of the image after geometric parameter optimization only. Ring artifacts are still very visible as are the beam hardening streak artifacts between the denser (brighter) objects. The combined effect of the gap between detectors and detector edge can be seen as the band encircling the whole object. 29

Figure 2-23. Reconstruction of the image after geometric parameter optimization and detector linearization. Effects of the detectors' gap were reduced by linear interpolation between the detectors. Beam hardening artifact's can still be seen. 30

Figure 2-24. Result of reconstructed test phantom after full optimization (linearization of detector and beam hardening correction). 30

Figure 3-1. Original Image (left) and its sinogram (right) for a parallel-beam scanner. For the sinogram image, the vertical axis shows the data position of the projection for a detector with 250 elements, and the horizontal axis shows the source position evenly incremented 250 times over 360^{o}. 32

Figure 3-2. Geometry of a source ray incident on a detector for fan-beam CT 33

Figure 3-3. Variation in position of a single point between parallel-beam and fan-beam. 34

Figure 3-4. Rotating frame of reference, where r is equivalent to y and s is equivalent to x at the initial source position $\beta=0^{o}$. 35

Figure 3-5: Typical motion-encoded data from an object in translational motion and the ideal sinusoid for the definite integral at each projection angle in radians. Each peak in the motion-encoded data represents a motion increment. 36

Figure 3-6. Motion-encoded data from an object in translation motion and the ideal curve for the center of mass vs. projection angle in radians. The simulated motion is from the same projection data used for Figure 3-5. 37

Figure 3-7. The relationship between (a) a single point located in the object space (i.e., xy coordinate plane) and (b) the same point in the sinogram space from $0 \leq \beta \leq 2\pi$ (adapted from [10]). 39

Figure 3-8. Reconstruction of the simulated image, uncorrupted by motion. 43

Figure 3-9. Simulation of the motion-free sinogram of the projections for the object shown in Figure 3-8. 43

Figure 3-10. Simulated motion-encoded sinogram image due to translational motion of the object during the scan. The motion-encoded sinogram contains a randomly assigned projection at each source position from 11 different sinograms obtained from 11 different translation positions with up to 5 mm offset. 44
Figure 3-11. Reconstructed image of the simulated motion-encoded sinogram matrix (Figure 3-10). 44
Figure 3-12. Sinogram image after applying the translational motion correction method to the sinogram shown in Figure 3-10. 45
Figure 3-13. Simulated motion-corrected reconstructed image of the motion-corrected sinogram matrix. 45
Figure 3-14. Visual representation of the point-by-point absolute value differences between the simulated reconstructed motion-free and motion-corrected images (Figures 3-8 and 3-12, respectively). The image has been inverted and contrast/brightness was adjusted to further highlight the differences. 46
Figure 3-15. Motion-free sinogram of the experiment phantom shown in Figure 2-24. .. 47
Figure 3-16. Motion-encoded sinogram simulating abrupt r-axis motion at $\beta = 90^{o}$. 48
Figure 3-17. Reconstructed image of the motion-encoded sinogram (Figure 3-16)..... 48
Figure 3-18. Motion-corrected sinogram of the motion-encoded sinogram (Figure 3-16). 49
Figure 3-19. Reconstructed image of the motion-corrected sinogram (Figure 3-18). 50
Figure 3-20. Visual representation of the point-by-point absolute value differences between the experimental reconstructed motion-free and motion-corrected images

(Figures 2-24 and 3-19, respectively). The image has been inverted, and contrast/brightness was adjusted to further highlight the differences. 50

Figure 3-21. Motion-encoded sinogram of experimental data simulating abrupt s-axis motion at $\beta = 180^{o}$ using experimental data. 51

Figure 3-22. Reconstructed image of the simulated motion-encoded sinogram matrix (Figure 3-21). 52

Figure 3-23. Sinogram image after applying the translational motion-correction method to the sinogram (Figure 3-21). 52

Figure 3-24. Simulated motion-corrected reconstructed image of the motion-corrected sinogram matrix (Figure 3-23). 53

Figure 3-25. Visual representation of the point-by-point absolute value differences between the experimental reconstructed motion-free and motion-corrected images (Figures 2-24 and 3-24, respectively). The difference image has been inverted. . 53

Figure 3-26. Differences of motion-free images of the object at various offset distances for both the simulated and experimental scanner data. 55

Figure 3-27. Construction of a sinogram to simulate motion using segments of 2 sinograms. 56

Figure 3-28. Fractional differences between motion-free and motion-corrected images with 50% of the scan taken at increasing offset distances of the phantom. The designation x’ indicates that the motion was in the x-direction and occurred when the majority of this motion was along the s-axis. 57

Figure 3-29. Fractional difference between motion-free and motion-corrected images with 50% of the scan taken at an offset distance of 4 mm of the phantom occurring at different times of the scanning process. 58
Figure 3-30. Fractional difference between motion-free and motion-corrected images with a 4 mm offset distance of the phantom for increasing amounts of motion-subjected times during the scan. 59

1. Introduction

There are many factors that can degrade the quality of a reconstructed image in computed tomography (CT). Some are artifacts caused by system errors whereas others are the effect of patient motion during the scanning process. The former problem can be reduced by optimizing the system. The latter can be reduced by developing motion correction techniques.

1.1 Description of the System

The system that is optimized in this paper is a focal High Resolution Computed Tomography (fHRCT) scanner. The system utilizes third-generation CT techniques for scanning yet retains the translation function of a second generation CT scanner. It consists of a single source with a voltage range of 0-50 kVp and a current range of 0-1 mA. Two equidistant linear detectors with 1024×512 elements are abutted lengthwise, with a gap between them of approximately 50 elements, creating a single detector with 2098×512 elements. However, only a single detector row (2098×1 elements) is used in this project as the current interest is in 2D fan-beam reconstructed images. The linear detector elements are 50×50 microns in area. The source is purposefully tilted to increase the field of view, and the effects on the fan-beam geometry can be seen in Figure 2-1. To avoid issues with the gap between the two detectors, we limited our imaging projects to data received by only one of the detectors, which was approximately centered on the

cone-beam. After optimization, the system has an effective reconstruction area of approximately 2.7 cm in diameter.

1.2 Scanner Optimization

There are several causes for artifacts from insufficiently optimized systems. The three main problems are first, establishment of the necessary mechanical parameters that are required to correctly reconstruct an image. Unlike the methods for detector calibration and beam hardening, the method used here is not standard, as the translation function is exploited to help determine these parameters. Second, the detector must be calibrated to remove the ring artifacts present in the reconstructed image. And third, beam hardening correction is applied to the linearized data to reduce cupping and streaking. These optimizations are necessary for the motion correction to be effective.

1.3 Patient Motion Correction

For the fHRCT scanner to take high resolution images, the time required for a scan is approximately three minutes. Because of this extended length of time, motion of the patient will be difficult to avoid, and the effect of that motion can greatly degrade the quality of a reconstructed image. Correcting for translational motion is the main concern. There are several methods to reduce this motion so that a scan can still produce a useful reconstructed image. Many of these were first developed for parallel-beam CT scanners, and many others use surface markers to determine the amount of motion. However, one of the primary goals of this project was to develop an algorithm for the fan-beam scanner that did not rely on surface markers. Therefore, a method that corrects translational motion is presented that makes use of the integral and center of mass of each projection as indicators of motion.

2. Optimization of System for Reduction of Scanner Artifacts

2.1 Parameter Calculation

Mechanical parameters in a fan-beam computed-tomography scanner are difficult to determine when these parameters are not mechanically established in advance. The important parameters to be determined of the fan-beam CT scanner are source-to-center-of-rotation distance, source-to-detector center distance, and detector center. In ideal cone-beam CT scanners, the beam from the source that traverses the center-of-rotation also intersects the detector at an angle normal to the detector surface.

When these parameters are not mechanically pre-established for a given CT scanner, they must be estimated. Both parallel-beam and fan–beam scanners use a pin of highly attenuating material as a marker for this determination. In parallel-beam CT, the pin is analyzed at two views taken 180^o apart from each other. The centroid of the pin in each of these views is calculated from the profile at these views, and the midpoint between the centroids denotes the position of the source at which the beam passes the center-of-rotation [1]. Due to the geometry of the fan-beam, this is not a practical way to determine the center-of-rotation. Common practice for a third-generation CT scanner is to take a full scan of a pin located at (x_o, y_o) and then determine the parameters based on the chi-square reduction of Equation 2.1 [1].

$$p(\beta) = D(x_o \cos\beta + y_o \sin\beta - \tau)/(x_o \sin\beta - y_o \sin\beta + Ro) + c \quad (2.1)$$

The variable p is the centroid of a projection of a pin at (x_o, y_o) at the gantry angle β. Figure 2-1 shows the fan-beam geometry of the fHRCT scanner with a displaced center-of-rotation, where the midline of the detector does not traverse the center-of-rotation.

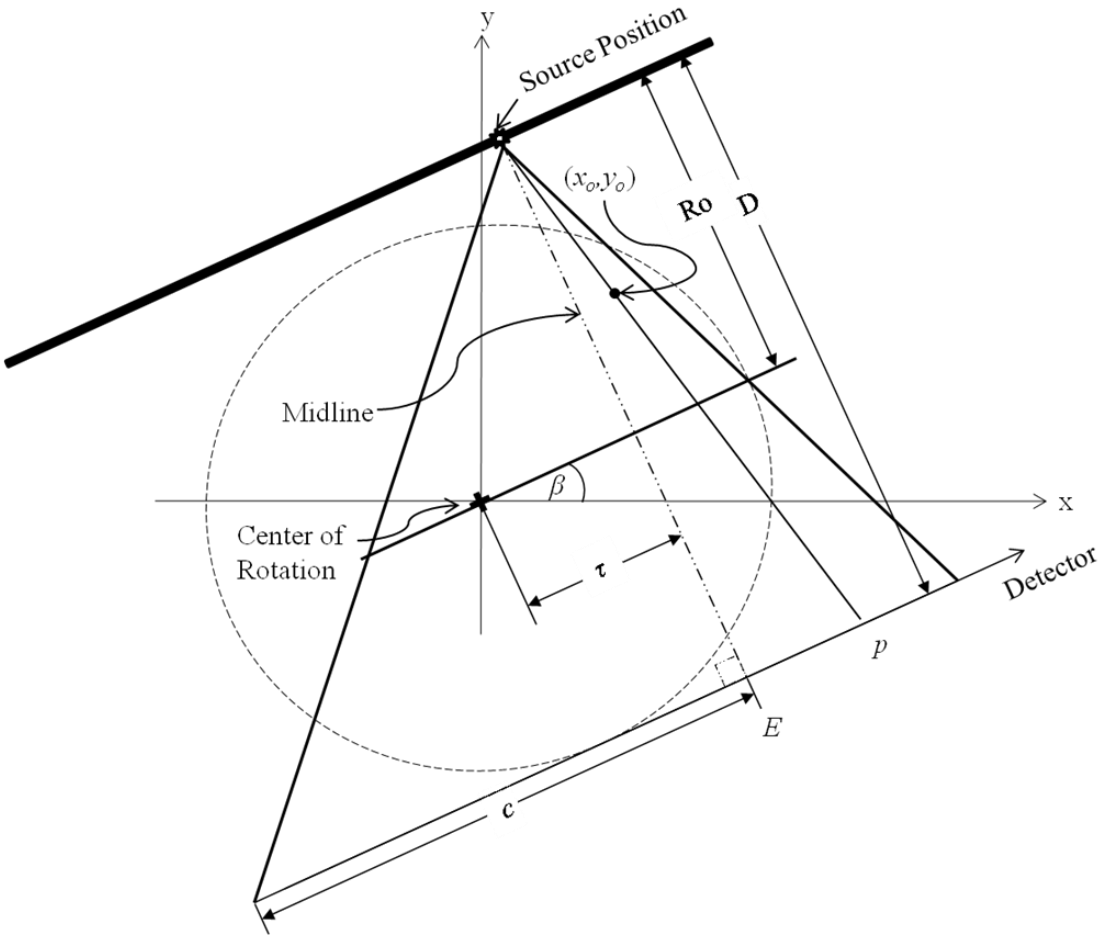

Figure 2-1. Fan-beam geometry with a midline offset from the center-of-rotation at gantry angle *β*. (adapted from [1])

D is the source-to-detector distance along the midline of the fan-beam, *Ro* is the source-to-center distance along the midline, *c* is the distance from the edge of the measurable

detector region to the detector element *E*, where *E* represents the position on the detector (i.e. the detector element) that the midline is incident, and τ is the offset of the midline from the center-of-rotation. The variable *c* can be calculated from *E* by $c = E \times$*(detector element length)*. Due to the six parameters that are solved for by the chi-square reduction, this process can yield inaccurate results. In the second/third-generation hybrid fHRCT scanner, the parameter calculation can be done in a multistep process that makes use of two full third generation scans of the pin point source and four subsequent translational scans utilizing the second-generation functionality of the scanner. From the data obtained from these six scans, the necessary parameters of *Ro*, *D*, *E* and τ, can be estimated to perform an accurate reconstruction.

2.1.1 Method for Parameters Calculation

To begin, the pin must be placed in the scanner's field of view. The pin can be placed anywhere within this region as long as it can be viewed at all angles. This position is designated as (x_o, y_o). Two full 360^o scans must be taken, where the translated positions of the source are not identical for both scans (i.e., two different values of τ). Figure 2-2 shows an ideal example of the projection of the pin at position (x_o, y_o) but with different τ's for Centroid A and Centroid B, and the position of *E* is represented by detector element 0. This yields two sinograms of the pin that can be used to determine at which angle the line defined by the pin and the center-of-rotation is parallel to the translation vector of the source and detector. Figure 2-3 shows an example of this line and how the distances between the rays that pass through the pin from translational source positions 1 and 2 at the arbitrary gantry angle β_i and $\beta_i+\pi$ (d_1 and d_2 in Figure 2-3a and 2-3b, respectively) are not equivalent. However, at the special angles β_{normal} and $\beta_{normal} + \pi$, this

line is perpendicular to the midline, and the distances between these rays (d_1 and d_2 in Figure 2-4a and 2-4b, respectively) are the same.

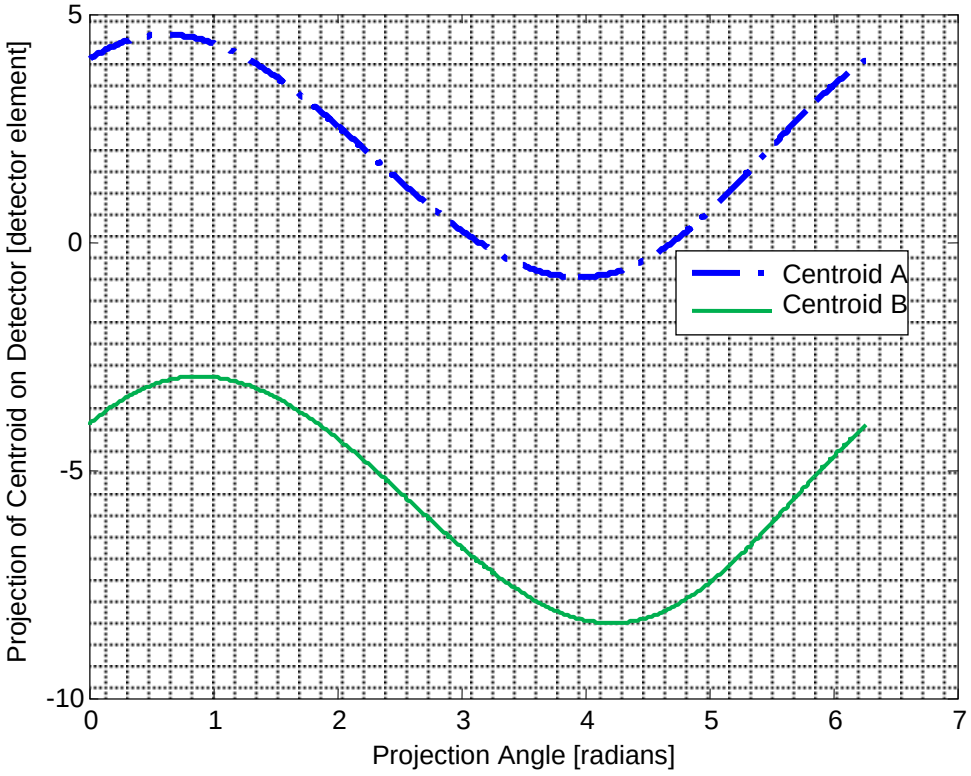

Figure 2-2. Centroid of the pin for two full third-generation scans. Centroid A and Centroid B show the centroid of a pin located at (x_o, y_o) at differing midline offset values τ. E for this example is detector element 0.

The process to determine β_{normal} and $\beta_{normal} + \pi$ is the comparison of the sinograms, at which the difference between Centroid A and Centroid B in Figure 2-2 is calculated for all projection angles β (Equation 2.2).

$$\Delta AB(\beta) = A(\beta) - B(\beta) \tag{2.2}$$

where A = Centroid A and B = Centroid B represent the centroid calculation at each projection angle β for the two translation positions τ_1 and τ_2 (Figure 2-5).

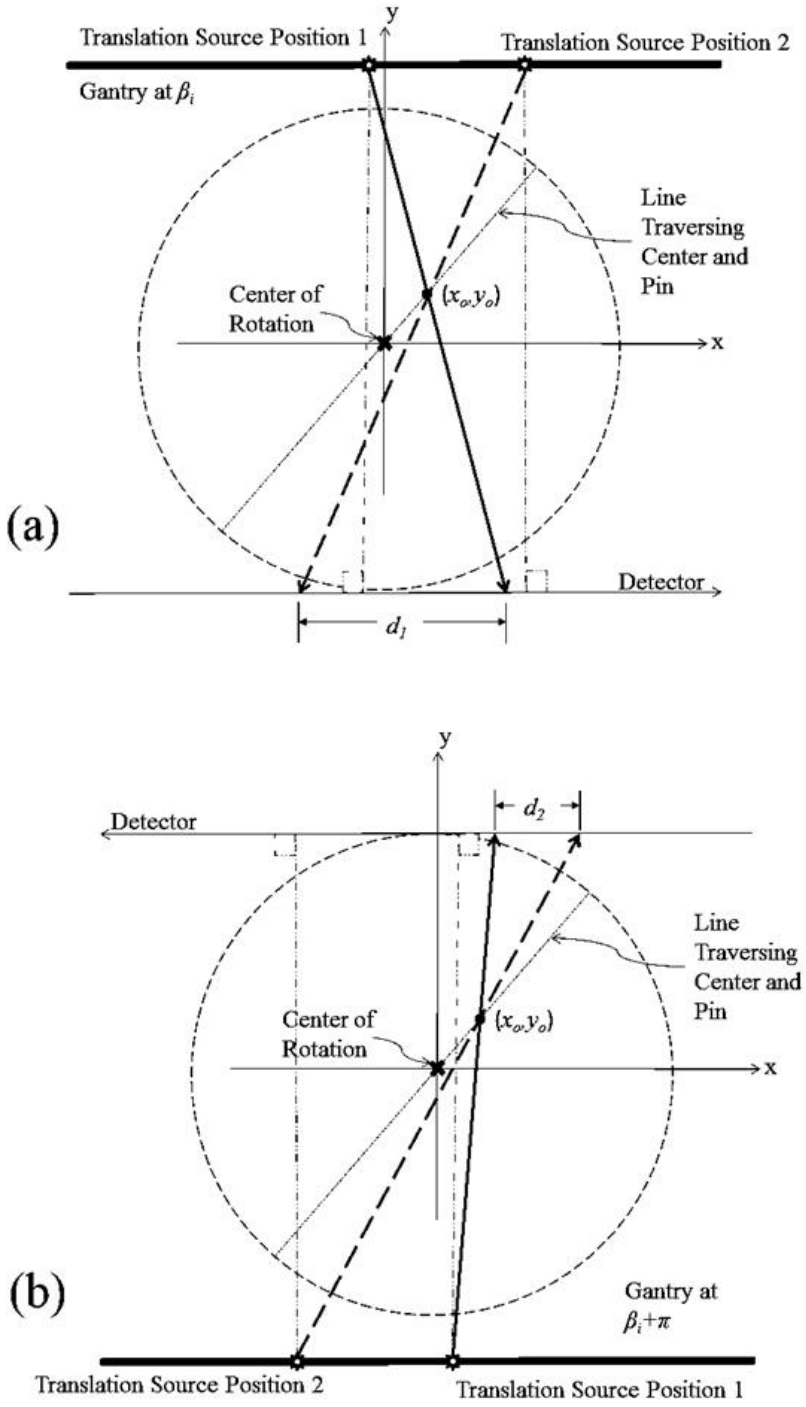

Figure 2-3. The difference of the rays incident on the pin from the two translation positions. (a) shows the difference as d_1 given the gantry angle at arbitrary position β_i and (b) shows the difference as d_2 given the complementary gantry angle of β_i, $\beta_i+\pi$. The midlines of the sources are not perpendicular to the line that traverses the center-of-rotation and the pin. Therefore $d_1 \neq d_2$. The detector is assumed to be fixed for simplicity.

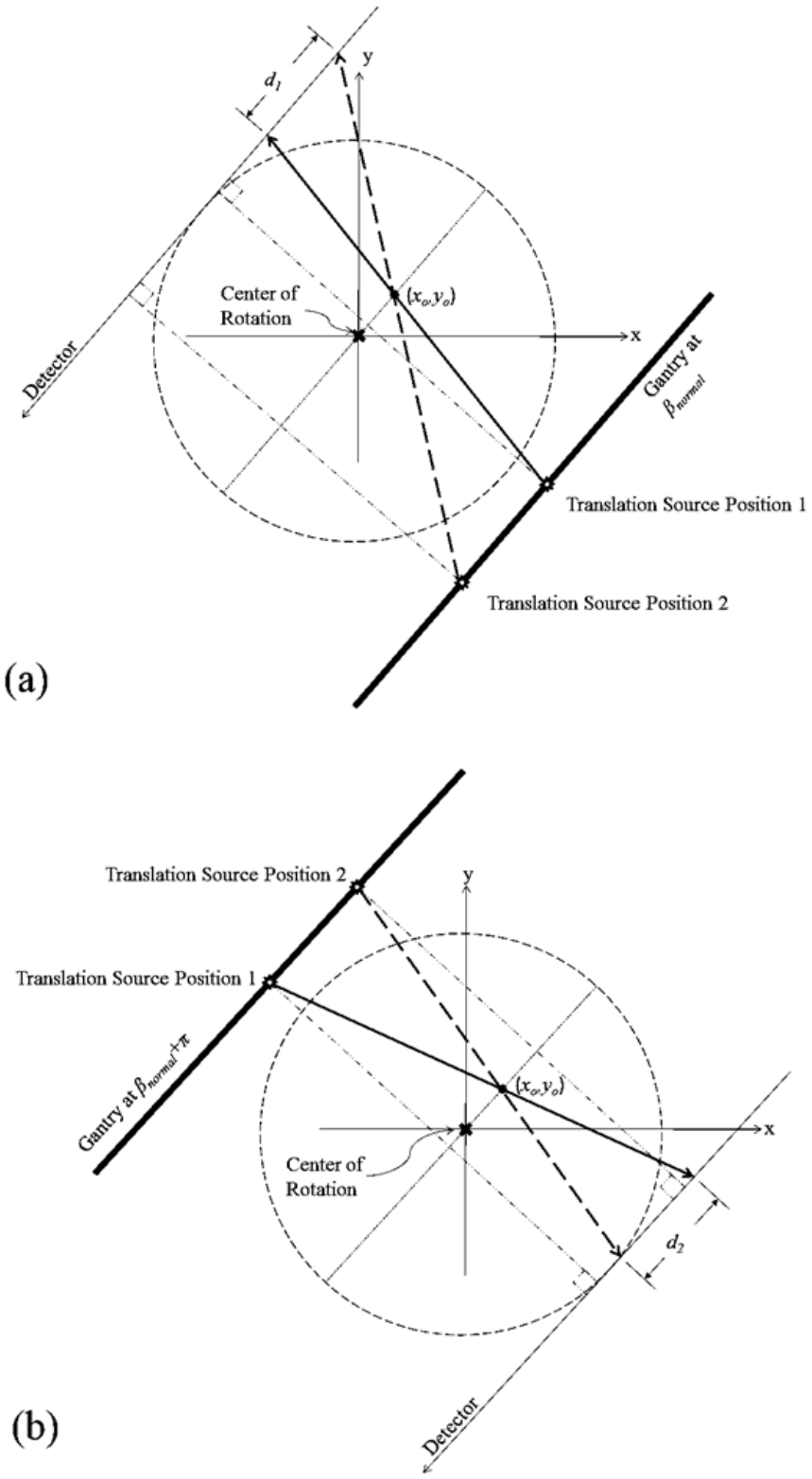

Figure 2-4. The difference of the rays incident on the pin from the two translation positions. (a) shows the difference as d_1 given the special gantry angle of β_{normal} and (b) shows the difference as d_2 given the complementary gantry angle of $\beta_{normal}, \beta_{normal}+\pi$. The midlines of the sources are now perpendicular to the line that traverses the center-of-rotation and the pin. Therefore $d_1=d_2$. Again, the detector is assumed to be fixed for simplicity.

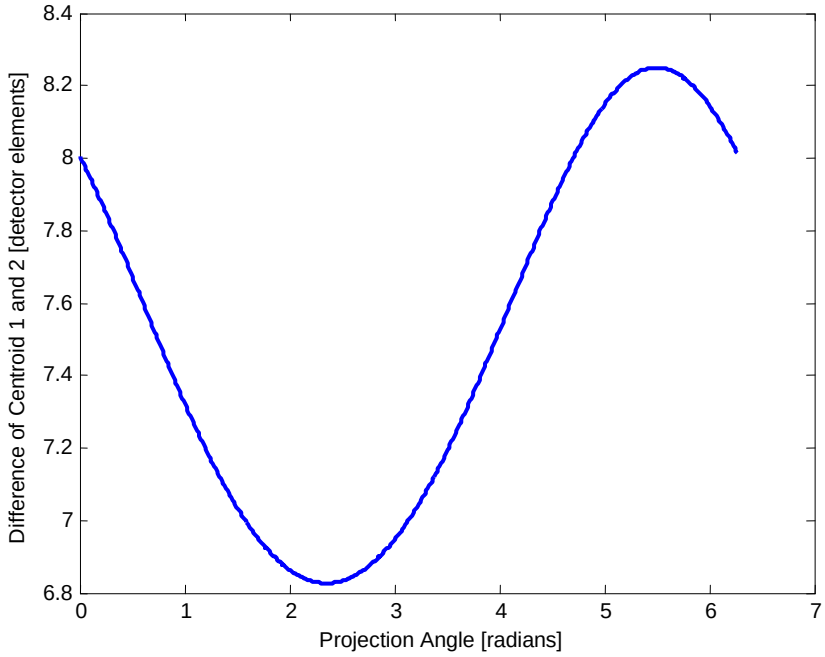

Figure 2-5. Difference between Centroid A and Centroid B at all projection angles.

For $0 \leq \beta < \pi$ the absolute difference of $\Delta AB(\beta)$ and $\Delta AB(\beta+\pi)$ is then calculated (Equation 2.3).

$$\beta_{normal} = \min\left(|\Delta AB(\beta) - \Delta AB(\beta + \pi|\right) \qquad (2.3)$$

The angle β, at which the absolute difference reaches a minimum, determines the angle for which the fan midline is perpendicular to the line that traverses the pin and the center-of-rotation shown in Figure 2-4. Figure 2-8 shows the result of Equation 2.3. Inspection of Figure 2-6 shows that only one such minimum exists as long as $(x_o, y_o) \neq (0, 0)$.

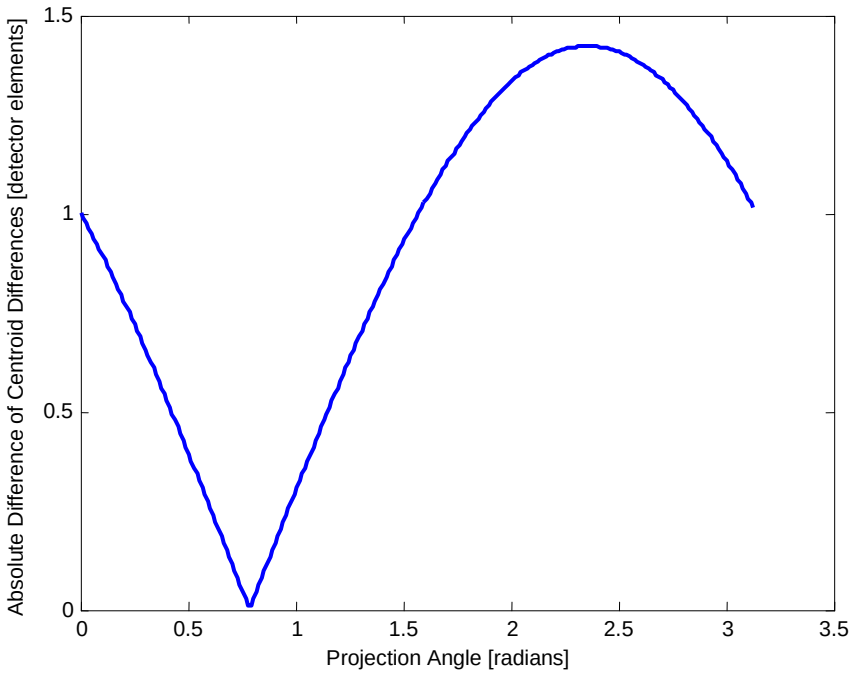

Figure 2-6. Absolute difference of $\Delta AB(\beta)$ and $\Delta AB(\beta+\pi)$ for $0 \leq \beta < \pi$.

The position *E*, where the midline is incident on the detector, and the position of τ=0 for the midline can now be determined simultaneously by taking two second-generation translation scans at $\beta_{normal} + \pi/2$ and $\beta_{normal} - \pi/2$ (Figure 2-7).

With the scanner at this position, the midline is now parallel to the line that traverses the pin and the center-of-rotation. Therefore, only when the midline (Figure 2.1) crosses the center-of-rotation (i.e. when $\tau = 0$) will results of the translation scans at $\beta_{normal} + \pi/2$ and $\beta_{normal} - \pi/2$ have the same centroid position of the pin incident on the detector translation position. The translation positions of the source vs. projection of the pin for the translational scan at $\beta_{normal} + \pi/2$ and $\beta_{normal} - \pi/2$ are plotted together, and the intersection

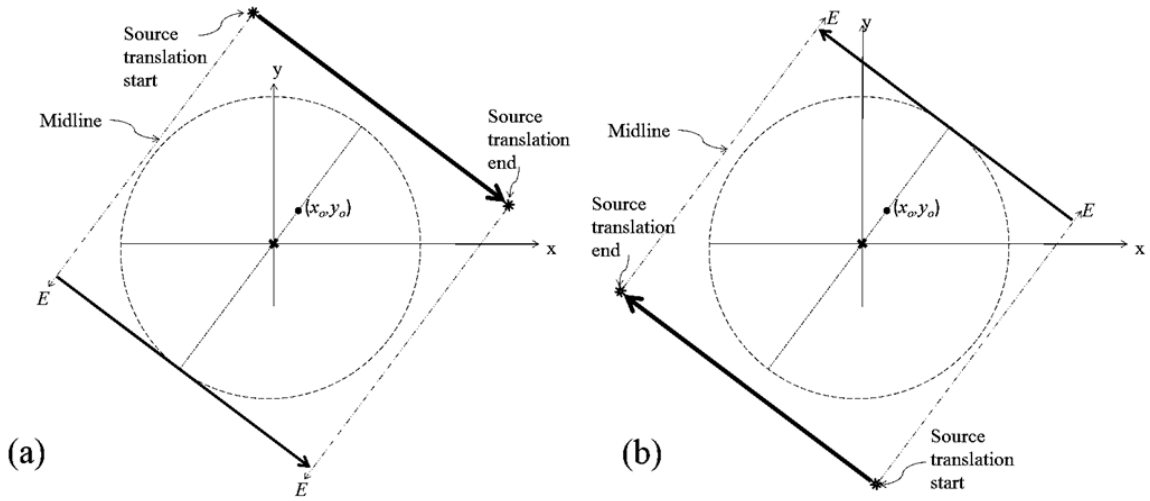

Figure 2-7. The translation scan taken at (a) $\beta_{normal} + \pi/2$ and (b) $\beta_{normal} - \pi/2$, where the midline for each is paralle1 to the line that traverses the center-of-rotation and the pin.

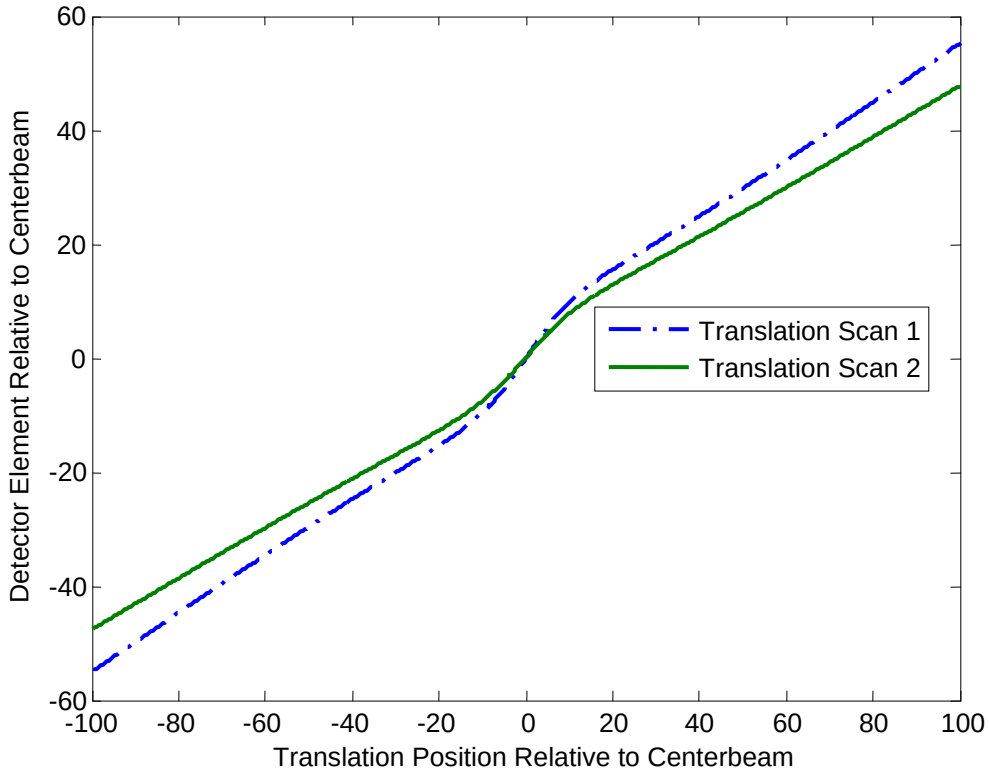

Figure 2-8. The projection of the pin vs. translation position of the source for the translational scan at $\beta_{normal} + \pi/2$(Translation Scan 1) and **$\beta_{normal} - \pi/2$(Translation Scan 2).**

of these two plots gives both the translation position where $\tau = 0$ and the detector element E (shown to be the given value of 0 from Figure 2-2). Figure 2-8 shows the general shape

of two plots of the projected pin position on the detector at differing positions of τ for an equidistant detector.

After the scanner translation position where $\tau = 0$ and the value of E at this position are estimated, the remaining parameters of D and Ro (Figure 2.1) can be estimated given two more translational scans at β_{normal} and $\beta_{normal} + \pi$ (Figure 2-9). Figure 2-10 shows the result of two such scans, from which the distance of the pin from the center-of-rotation can be determined. The difference in the translation positions where the centroids of the pin at β_{normal} and $\beta_{normal} + \pi$ are at the detector element E gives the result of twice the object-to-center-of-rotation distance OC.

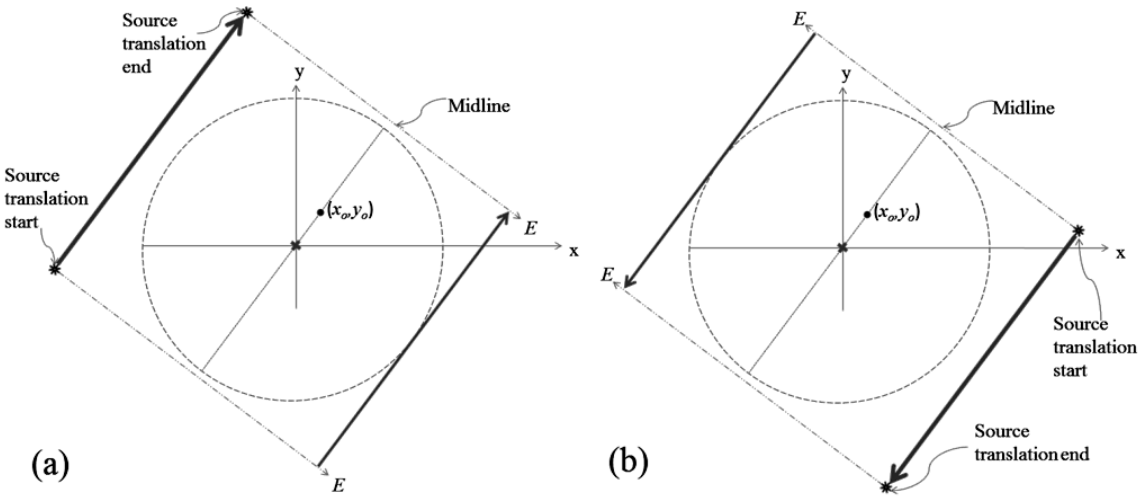

Figure 2-9. The translation scan taken at (a) β_{normal} and (b) $\beta_{normal} + \pi$, where the midline for each is perpendicular to the line that traverses the center-of-rotation and the pin.

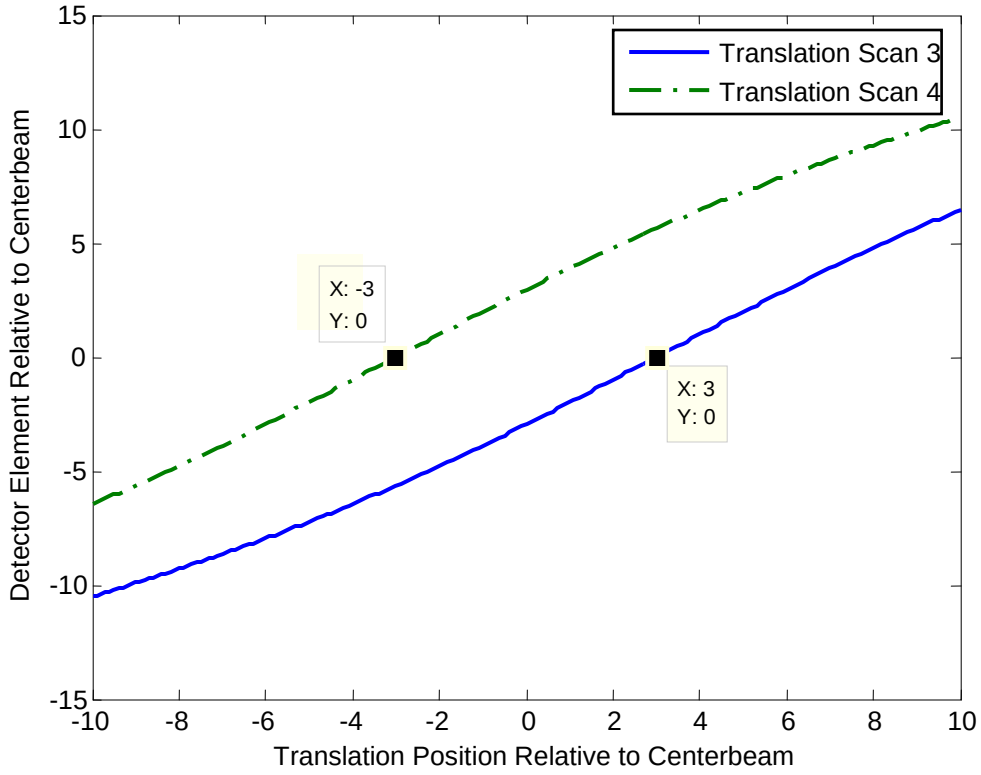

Figure 2-10. The translation position of the source vs. projection of the pin for the translational scan at β_{normal} and $\beta_{normal} + \pi$. In this instance the Euclidean distance is 6 units and, consequently, the pin is 3 units from the center.

Utilizing the data obtained from the translational scans at $\beta_{normal} + \pi/2$ and $\beta_{normal} - \pi/2$ again, the slopes of Translation Scan 1 and Translation Scan 2 can be estimated near the midline position on the detector E. Due to magnification, the change in centroid position on the detector has an essentially linear response as the translation position of the midline of the source crosses this point. This can be seen by zooming in to the intersection point in Figure 2-8, and this shown in Figure 2-11. The values Δ_1 and Δ_2 are assigned to the slopes of Translation Scan 1 and Translation Scan 2 in this linear region, where Δ_1 is assigned to the greater slope for later calculation. Also, a linear fit can be helpful to determine these slopes. Given the size of each detector element, Δ_1 and Δ_2 should be converted from element per translation distance to distance per distance.

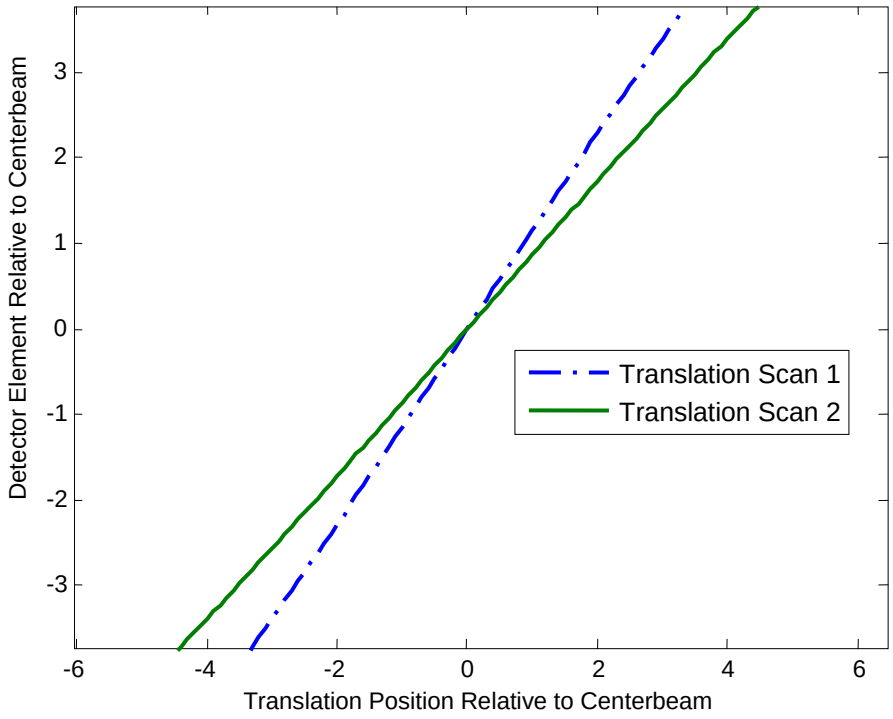

Figure 2-11. Linear region of Figure 2-8 showing the projection of the pin vs. the translation position of the source for the translational scan at $\beta_{normal} + \pi/2$ and $\beta_{normal} - \pi/2$.

Within this linear region, the angles α_1 and α_2 (Figure 2-12) that the line from the source through the centroid position creates with the midline can be estimated at $\beta_{normal} + \pi/2$ and $\beta_{normal} - \pi/2$ with Equations 2.4 through 2.15. Figure 2-12 shows the geometric relationships that can be used to solve for the remaining parameters *D* and *Ro*, where *Rd* is the center-of-rotation-to-detector distance, and *TR* is the translation of the midline.

$$\alpha_1 = \tan^{-1}\frac{TR}{Ro - OC} \tag{2.4}$$

$$\alpha_1 = \tan^{-1}\frac{\Delta_1 \cdot TR}{D} \tag{2.5}$$

$$\alpha_1 = \tan^{-1}\frac{\Delta_1 \cdot TR}{Ro + Rd} \tag{2.6}$$

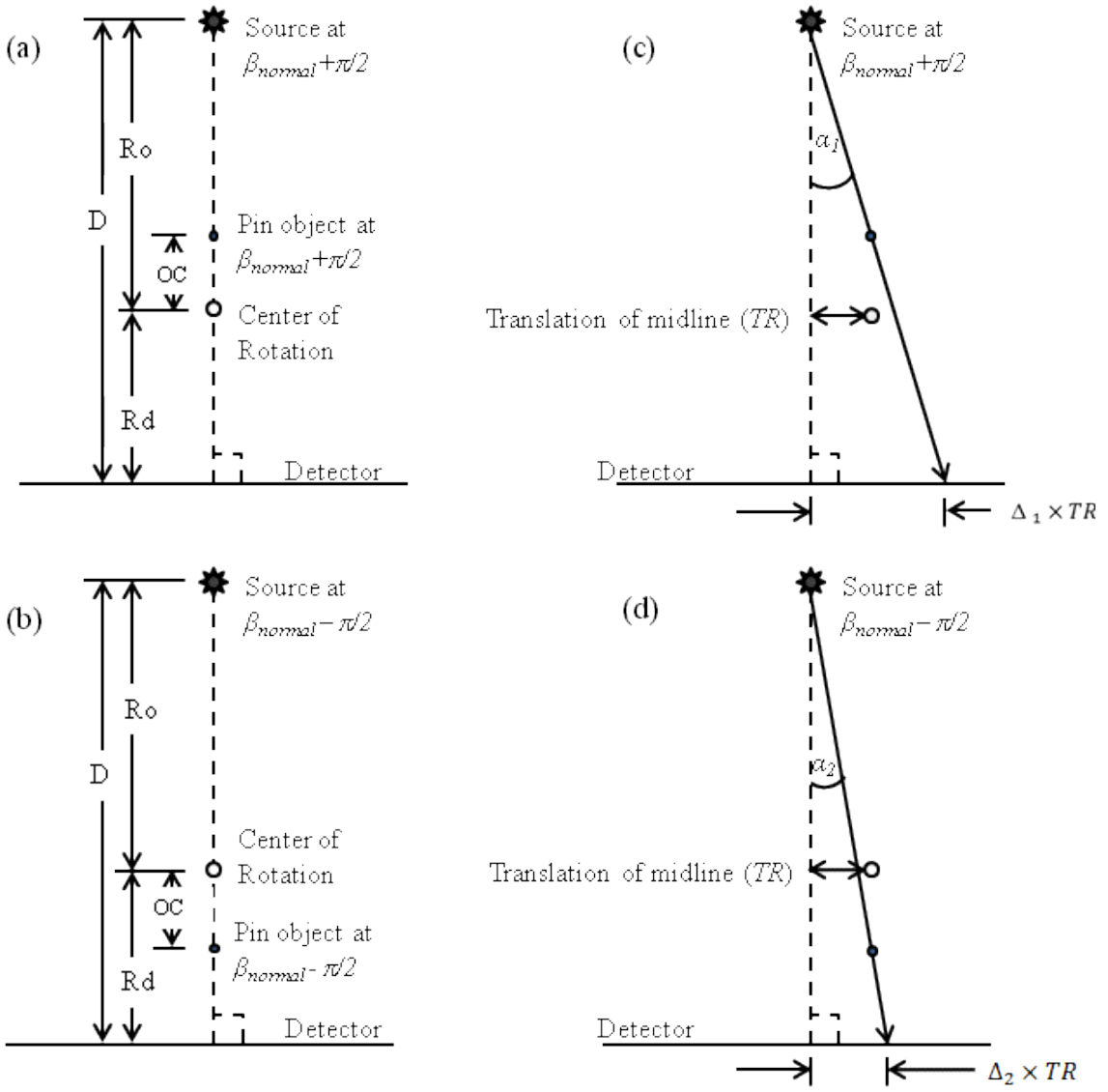

Figure 2-12. The geometric relationships used to determine the parameters *D* and *Rd* where (a) shows the position of the pin at $\beta_{normal} + \pi/2$, (b) shows the position of the pin at $\beta_{normal} - \pi/2$, (c) shows the effect of a translation of the source on the projection of the pin on the detector given the source at $\beta_{normal} + \pi/2$, and (d) shows the effect of a translation of the source on the projection of the pin on the detector given the source at $\beta_{normal} - \pi/2$.

$$\alpha_2 = \tan^{-1}\frac{TR}{Ro + OC} \tag{2.7}$$

$$\alpha_2 = \tan^{-1}\frac{\Delta_2 \cdot TR}{D} \tag{2.8}$$

$$\alpha_2 = \tan^{-1}\frac{\Delta_2 \cdot TR}{Ro + Rd} \tag{2.9}$$

With these equations, two equations of D can be determined by setting Equation 2.4 equal to Equation 2.5 as well as setting Equation 2.7 equal to Equation 2.8to yield:

$$D = \Delta_1(Ro - OC) \tag{2.10}$$

$$D = \Delta_2(Ro + OC) \tag{2.11}$$

Setting Equation 2.10 equal to Equation 2.11, the value of Ro can be determined given that OC, Δ_1, and Δ_2 are known. This is shown in Equations 2.12a through 2.12b.

$$\Delta_1(Ro - OC) = \Delta_2(Ro + OC) \tag{2.12a}$$

$$Ro = OC\frac{\Delta_1 + \Delta_2}{\Delta_1 - \Delta_2} \tag{2.12b}$$

After *Ro* is obtained, the equation for determining *Rd* can be solved by either setting Equation 2.4 equal to Equation 2.6 or setting Equation 2.7 equal to Equation 2.9. Equations 2.13a through 2.13c show the result of solving for *Rd* after setting Equation 2.4 equal to Equation 2.6.

$$\frac{TR}{Ro - OC} = \frac{\Delta_1 \cdot TR}{Ro + Rd} \tag{2.13a}$$

$$Ro + Rd = \Delta_1(Ro - OC) \tag{2.13b}$$

$$Rd = \Delta_1(Ro - OC) - Ro \tag{2.13c}$$

Thus, the equations to determine the magnitude of *Ro* and *Rd* are as follows:

$$Ro = \left|OC\frac{\Delta_1 + \Delta_2}{\Delta_1 - \Delta_2}\right| \tag{2.14}$$

$$Rd = |\Delta_1(Ro - OC) - Ro| \tag{2.15}$$

The source-to-detector distance along the midline is $D = Ro+Rd$.

2.1.2 Parameter Calculation Results

Figure 2-13 shows the results of two real full 360 degree scans at differing translational positions using the fHRCT. The figure shows the centroid positions of the pin where the pin is positioned at $(x_o, y_o) \neq (0, 0)$. Linear interpolation was used to artificially increase the number of projections from 500 to 500,000. This increased the precision of the calculated angle β_{normal}.

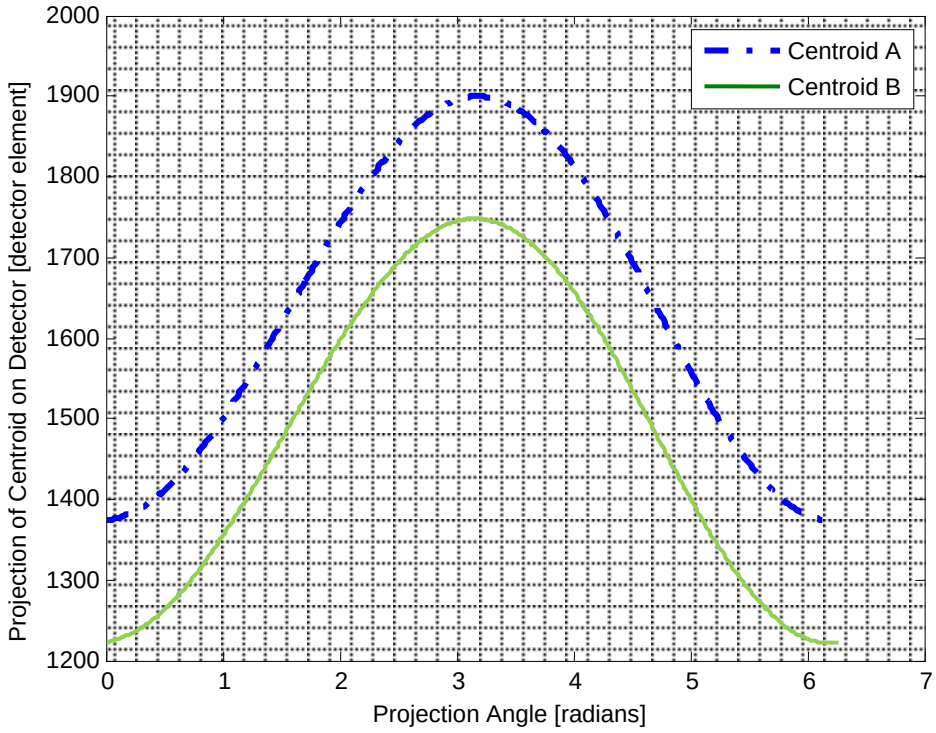

Figure 2-13. Centroid of the pin for two full third-generation scans. Centroid A and Centroid B show the centroid at differing midline offset values τ.

The difference ΔAB between Centroid A and Centroid B is calculated for all projection angles β (Equation 2.2). Figure 2-14 shows ΔAB at all angles β.

Employing Equation 2.3, the minimum of the absolute difference between $\Delta AB(\beta)$ and $\Delta AB(\beta+\pi)$ with the pin position used to graph Centroid A and Centroid B (Figure 2-15). This was repeated two more times, yielding three values of β_{normal}: 3.0894 rad, 3.0888 rad, and 3.0900 rad. The average of these were calculated, resulting in the values of β_{normal} to be 3.0894 rad (177.009^o) and $\beta_{normal} + \pi$ to be 6.231 rad (357.009^o), with a standard deviation of 0.00062 rad (0.035^o). After these gantry angles were determined, a translational scan was taken at $\beta_{normal} + \pi/2$ and $\beta_{normal} - \pi/2$. This results in Figure 2-16, where the intersection of the plots for Translation Scan 1 and Translation Scan 2 is at detector element 1286.185 and translation position 75.5753 mm. Therefore, the translation position of the source, where $\tau=0$, is 75.5753 mm, and the detector element that represents E is 1286.185.

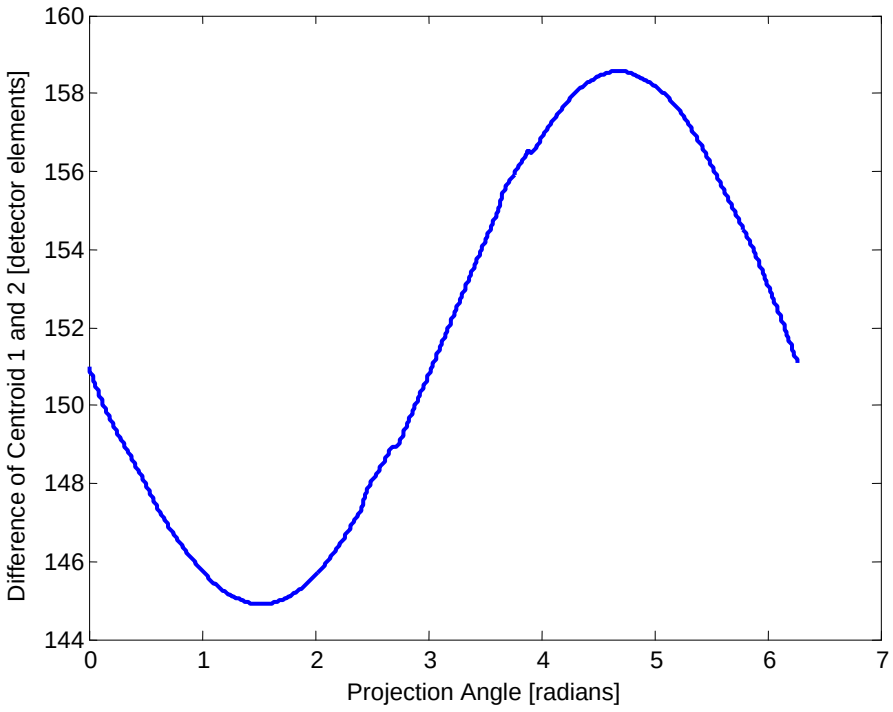

Figure 2-14. Difference between Centroid A and Centroid B at all projection angles.

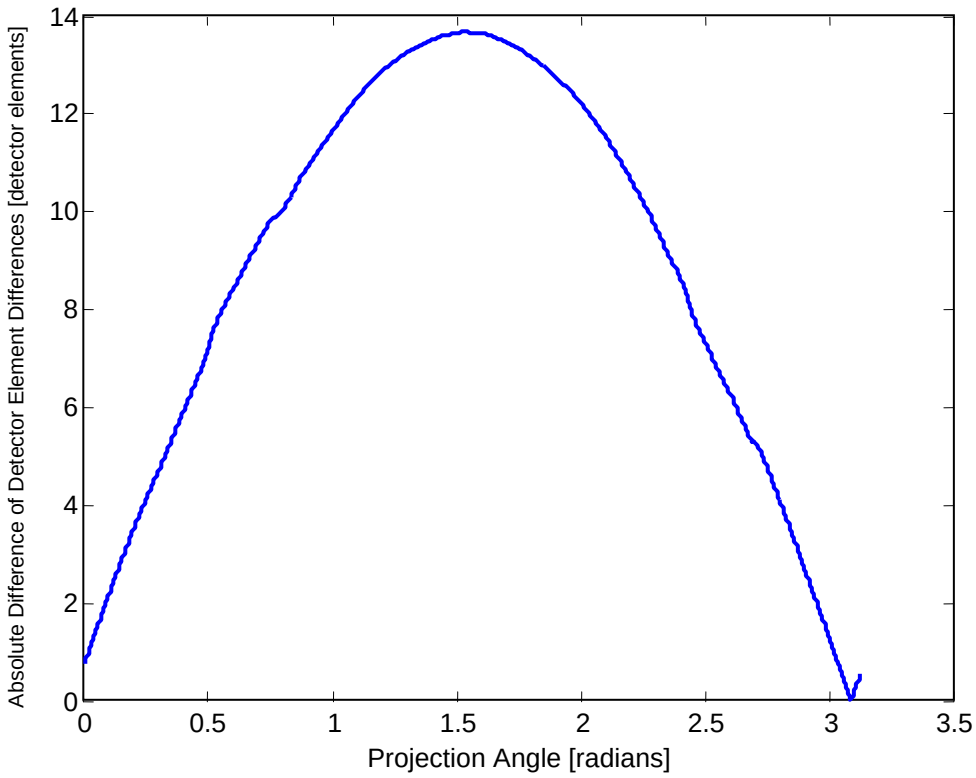

Figure 2-15. Absolute difference of $\Delta AB(\beta)$ and $\Delta AB(\beta+\pi)$ for $0 \leq \beta < \pi$.

After $\tau = 0$ and the value of E at this position were estimated, the remaining parameters of D and Ro were calculated given two more translational scans at β_{normal} and $\beta_{normal} + \pi$. The difference in the translation positions, where the centroids of the pin at β_{normal} and $\beta_{normal} + \pi$ are at the detector element E, gave the result of 18.048 mm. Accordingly, the object-to-center distance (OC) is 14.552 mm / 2 = 7.2762 mm. The values of Δ_1 and Δ_2, determined from the slopes of the linear fits for Translation Scan 1 and Translation Scan 2, are 39.76 elements/mm = 1.988 mm/mm and 36.21 elements/mm = 1.811 mm/mm, respectively. The parameter Ro was calculated by substituting OC, Δ_1, and Δ_2 into Equation 2.14.

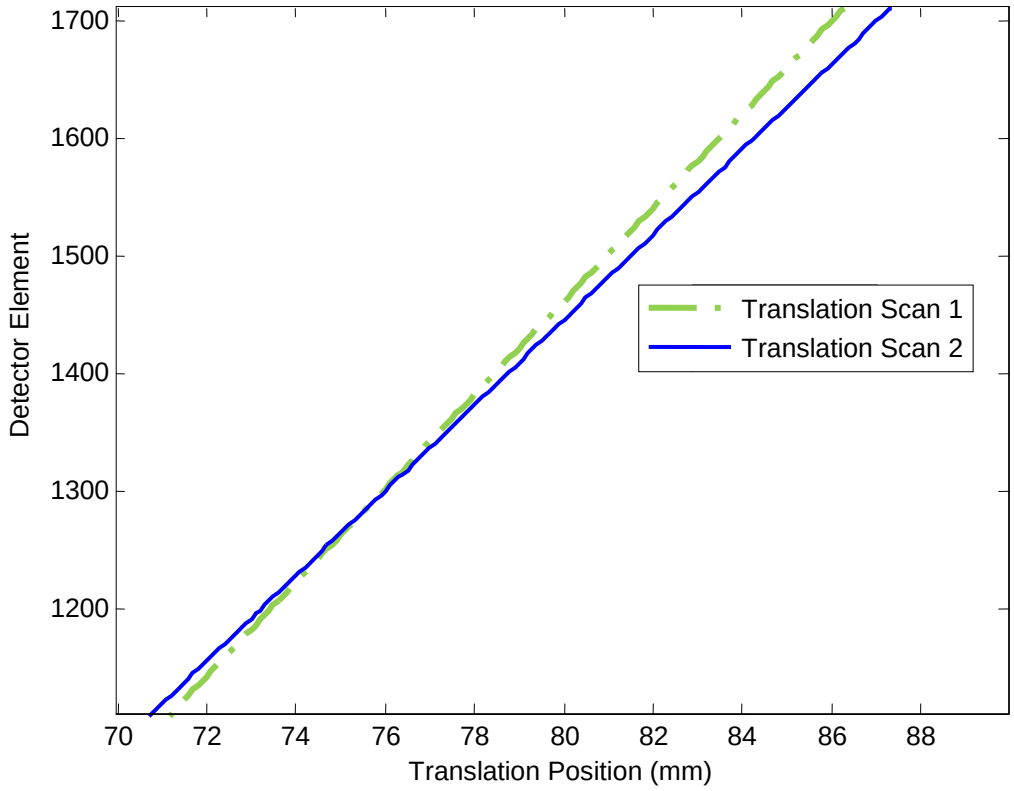

Figure 2-16. Linear region of the projection of the pin vs. the translation position of the source for the translational scan at $\beta_{normal} + \pi/2$ (data1) and $\beta_{normal} - \pi/2$ (data2).

After *Ro* was calculated to be 149.72 mm, *Rd* was subsequently determined by substituting *OC*, Δ_1 and the previously calculated *Ro* into Equation 2.15. *Rd* is 134.02 mm, and the sum of *Ro* and *Rd* yields the parameter *D* to be 283.75 mm.

2.2 Detector Linearization

Calibration of the detector is another important step in optimization of the fHRCT system. Each detector element of the solid state detector that is used in this system must be calibrated independently. The primary concern with an insufficiently calibrated detector is ring artifacts that appear in the reconstruction of a third-generation CT system [2, 3]. Ring artifacts are a result of miscalibration of a single, or multiple, detector elements that affect the projection at every angle of a rotation scan and, subsequently, the

reconstruction from these projections. This causes a ring or ripples to appear in the final image. Calibration by linearizing the detector effectively reduces or removes these artifacts. Linearization of the detector, also known as flat field correction, creates uniformity in the efficiency of the detector, such that the individual detector elements will show the same response when exposed to the same conditions [4].

2.2.1 Method for Detector Linearization

For simplicity's sake, the steps involved in detector linearization in the following will primarily discuss the process for a single element of the detector at row *i* and column *j*. The process is implemented concurrently for all other detector elements. At each source condition described, an average was taken by determining the mean of 100 readings at that condition.

First, the dark current value of the element is defined as the average response of the detector at a source condition of 0 mA of current for 0.5 seconds. This value is subtracted from each of the other conditions.

After the dark current value is established, the average data are collected at each current condition and a voltage of 46.875 kVp. Seventeen current conditions were used ranging from 0 mA to 1 mA, evenly incremented, all at a voltage of 46.875 kVp for 0.5 seconds. A second degree polynomial was fit through these 17 points, and the slope for the ideal linear response was estimated using the first 10 points of the data. The plot for these points along with the curve fit and the ideal linear response of the system can be seen in Figure 2-17. The quadratic fit shows a general increase in counts over the estimated ideal detector linear response due non-linearity. As this is a detector being operated in current

mode, the non-linearity can produce higher or lower detector readings at high photon flux.

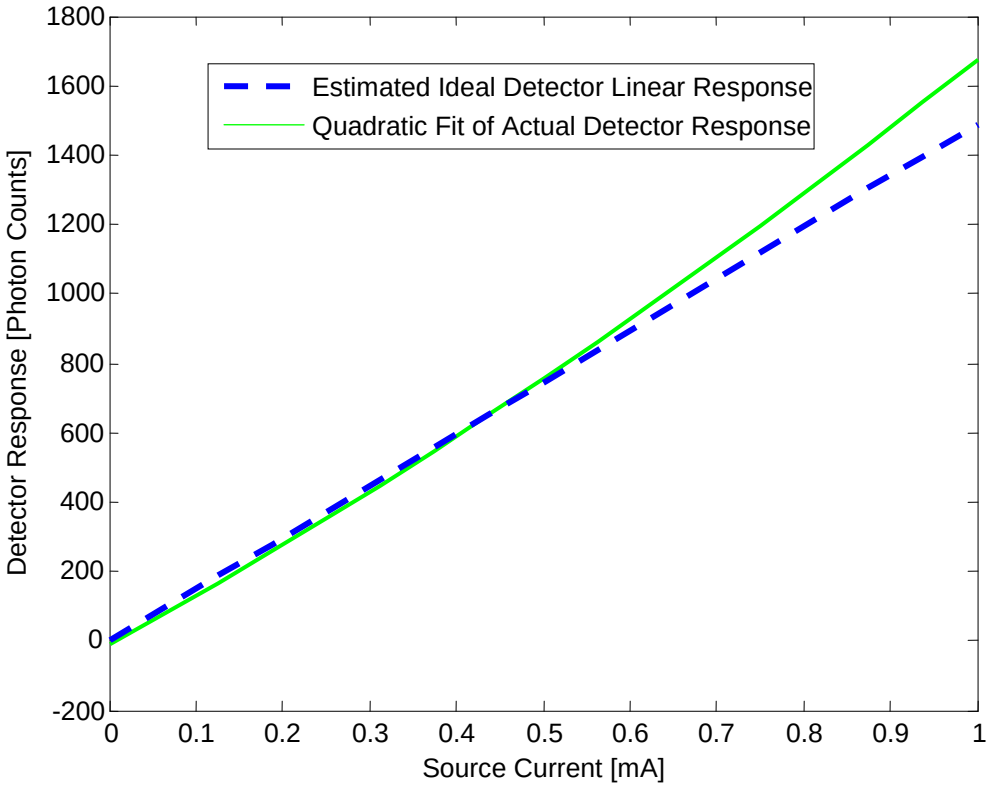

Figure 2-17. Graph showing the actual and ideal response of a representative detector element.

For the flat field correction, the ideal linear response should be the same for all detector elements. Therefore if the slope of the detector's i,j-th element ideal linear response is $m_{i,j}$, then m_{avg} is the average of $m_{i,j}$ at all detector elements i,j . Equation 2.15 shows the ideal number of counts, Y, as a function of the current, x. Equation 2.16 is the fit for the practical case where $a_{(i,j)n}$ are the coefficients of the quadratic fit for the detector element i,j.

$$Y = m_{avg}x \tag{2.15}$$

$$y(i,j) = a_{(i,j)2}x^2 + a_{(i,j)1}x + a_{(i,j)0} \tag{2.16}$$

By solving Equation 2.15 for x and substituting the results into Equation 2.16, the equation for correction of the value of $y(i,j)$, the practical counts, to the value of Y, the ideal case, can be obtained. This is shown in Equation 2.17.

$$y(i,j) = \frac{a_{(i,j)2}}{{m_{avg}}^2} Y^2 + \frac{a_{(i,j)1}}{m_{avg}} Y + a_{(i,j)0} \tag{2.17}$$

The real positive root of Equation 2.17 is the corrected value of $y(i,j)$ to the ideal value of Y.

Once the value of Y has been obtained and is inserted for the number of counts at each detector element, the detector data has been calibrated. This calibration is done for both the open field data N_o and the data for each projection N in a scan at source voltage 46.875 kVp and current 0.9375 mA.

The current can be changed without the need to change the calibration; however, a change in the tube voltage will require a new calibration function, and a new value of m_{avg} must also be calculated. Due to the slight fluctuations in tube output, even at a consistent current setting, the mean of an open field region of N (N_{avg}) for each detector reading was compared to the mean of the same region in N_o ($N_{o,avg}$). The value of N_o was adjusted by multiplying it by the ratio of these two means, $N_o' = N_o \times (N_{avg}/N_{o,avg})$. From here the value of $ln(N_o'/N)$ is determined and subjected to the beam hardening correction before final reconstruction.

2.2.2 Detector Linearization Results

The original raw data from the detector and the results of the linearization process for those raw data are shown for a single projection (Figure 2-18). Several variations from a flat field are evident in the image of the initial projection data, such as the gap between the detectors seen in the middle of raw data image (removed through interpolation in the linearization process), dead elements, and effects of the beam profile. The linearized projection has a considerably more uniform field, which is desired of an open field projection. The effect the linearization process has on the reconstructed image is shown in section 2.4 (Figures 2.22 and 2.23).

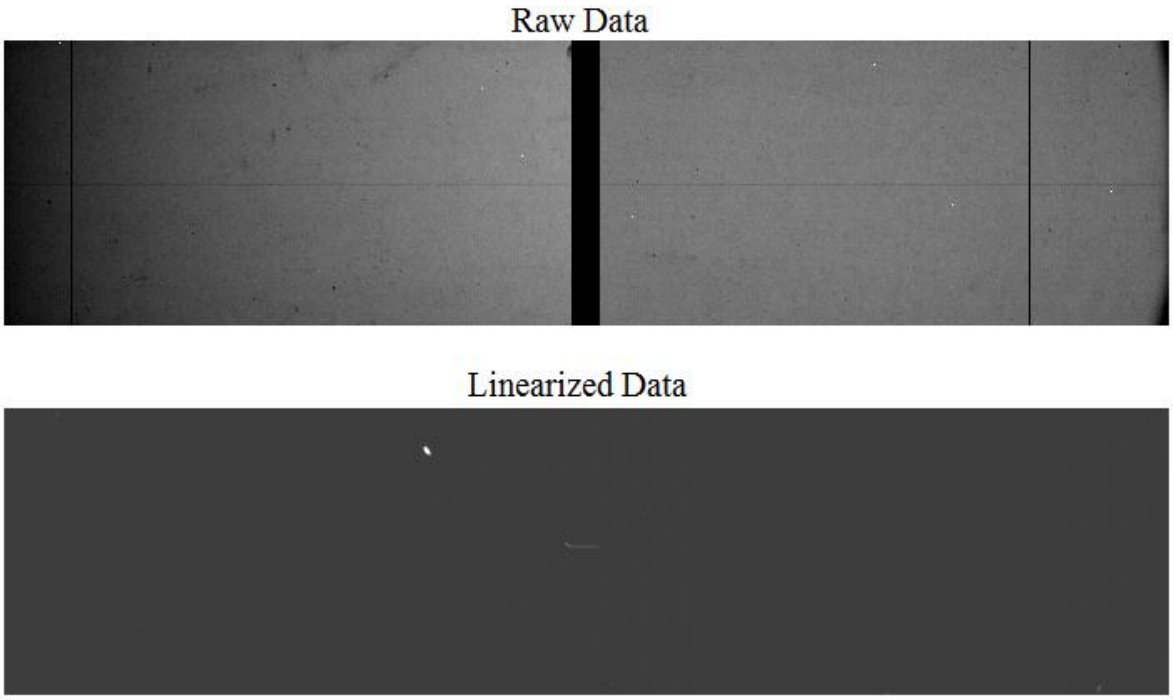

Figure 2-18. Two images of the same open field projection shown as (top) the raw data image and (bottom) the image of the linearized data. The bright spot in the linearized data indicates a collection of dead pixels in the detector.

2.3 Beam Hardening

In certain energy ranges, the linear attenuation coefficient for many materials decreases with energy. With a polychromatic x-ray beam, this causes the low-energy photons to be absorbed more readily, and the remaining beam has a greater proportion of high-energy photons [5]. Thus, as the beam passes through material, the average energy of the spectrum continues to increase. This causes larger numbers of photons to be incident on the detector than would be expected with a lower-energy mono-energetic beam. This phenomenon is known as beam hardening.

For the correction method described here, a preprocessing technique is used after the detector is linearized and before the reconstruction is executed. In this technique the assumption is made that, under ideal conditions, the measurement $ln(N_o/N)$ is linearly proportional to the thickness of a homogenous absorber, where N_o is the total number of photons entering the material and N is the number of photons exiting the material [5].

2.3.1 Method for Beam Hardening Correction

N_o was obtained from the average of all detector elements for an open field scan of 100 readings at a source voltage of 46.875 kVp and a current of 0.9375 mA as used in the motion-correction sequence described later. The values for N were determined the same way after an appropriate amount of homogenous material was placed in the path between the source and detector. The homogeneous material used in this correction was aluminum. The undisturbed condition was assumed to be the slope produced from the line through the results for 0 mm and 1 mm of aluminum and is given the variable m in Equation 2.18, where F is the ideal case of $ln(N_o/N)$ as a function of x, the total thickness

of aluminum (Figure 2-19). The actual values of $ln(N_o/N)$ for up to 10 mm of aluminum by increments of 1 mm are shown as the practical case in Figure 2-19.

The correction to each detector element was made by first fitting a curve through the results of the practical data. The best fit was calculated by forcing a 3rd degree polynomial using a least squares fit through the 11 data points obtained from the increasing number of plates. Equation 2.19 shows a general 3rd degree polynomial where *f*, the practical value of $ln(N_o/N)$, is depicted as a function of *x*, the total thickness of aluminum, and a_n represent the coefficients of the polynomial fit.

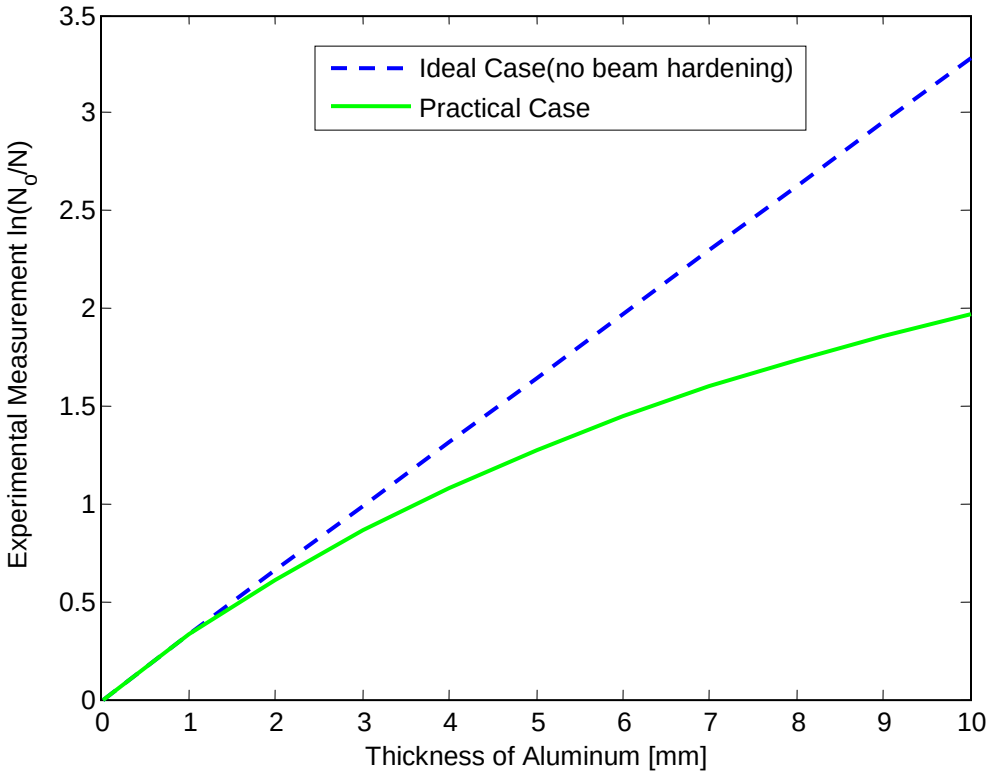

Figure 2-19. Graph of the actual and ideal response of the detector with increasing thickness of aluminum in the source-to-detector path.

$$F(x) = mx \tag{2.18}$$

$$f(x) = a_3x^3 + a_2x^2 + a_1x + a_0 \quad (2.19)$$

After the coefficients of the polynomial have been determined, the correction for each detector element *i,j* at each source angle can then be calculated. Given the value of $f_{i,j}(x)$, the value of *x* is calculated to find the analogous amount of aluminum representing this value of *f*. This is done by finding the positive real root for the 3rd degree polynomial. Finally, the calculated value of *x* is then inserted into Equation 2.18 to determine the value of *F*, the ideal value, to replace *f* at detector element *i,j*. This process is used for each detector element as the correction of the data for beam hardening.

2.3.2 Beam Hardening Correction Results

The beam hardening correction produced favorable results. While all projection values are affected by the correction method, it can be seen that the lower projection values (i.e. those below 0.5) are marginally affected by the correction method. The higher values, which are more likely affected by beam hardening, are increased by the method described earlier to compensate for the increased attenuation of lower energy photons through thicker and denser materials. Figure 2-20 shows the results of the correction for a single projection. The qualitative effects are more easily seen after reconstruction of the images and are shown in the following section (Figures 2-23 and 2-24).

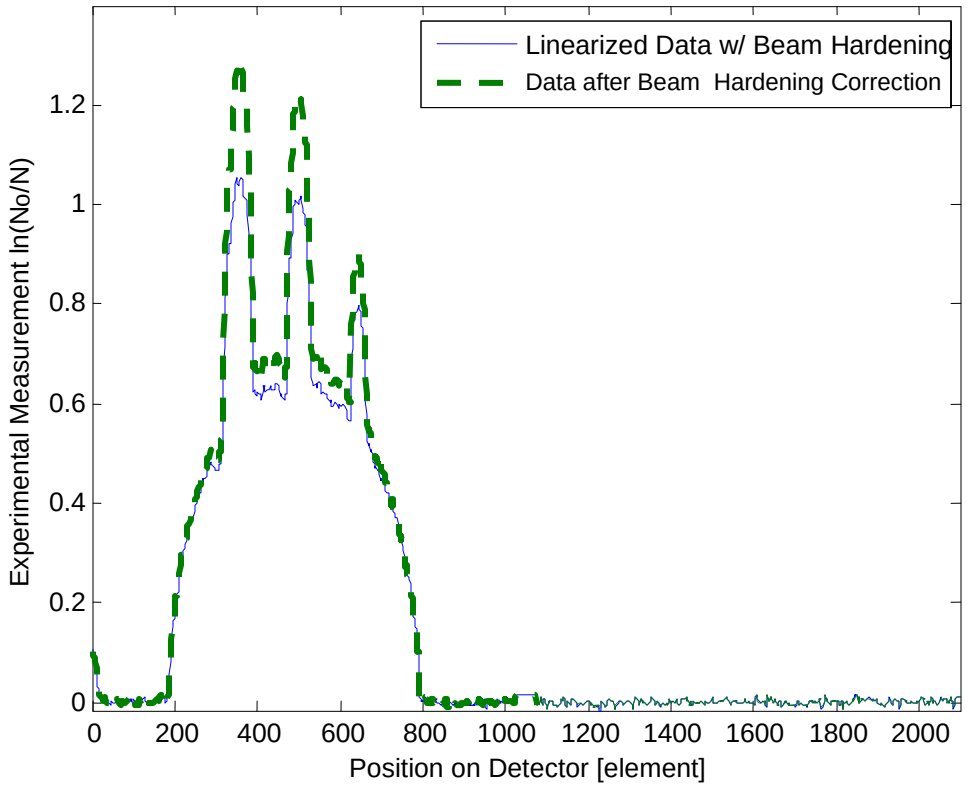

Figure 2-20. Graph of the linearized data before and after correction for beam hardening.

2.4 Reconstruction and Results

To increase the field of view, the source position was intentionally moved to 84 mm causing an offset value τ of 8.4247 mm. After iteratively adjusting the value of E around 1286.2, it was determined that changing the value of E from 1286.2 to 1289.2 qualitatively improved the reconstruction image. Generally, the artifacts indicative of an incorrect parameter value (e.g. doubling of edges) was reduced, and overall sharpness of the image was improved. The fan-beam reconstruction algorithm for a midline displaced from the center-of-rotation was used to produce the images in Figures 2-21 through 2-24 [6]. Overall, the optimization was determined to be acceptable.

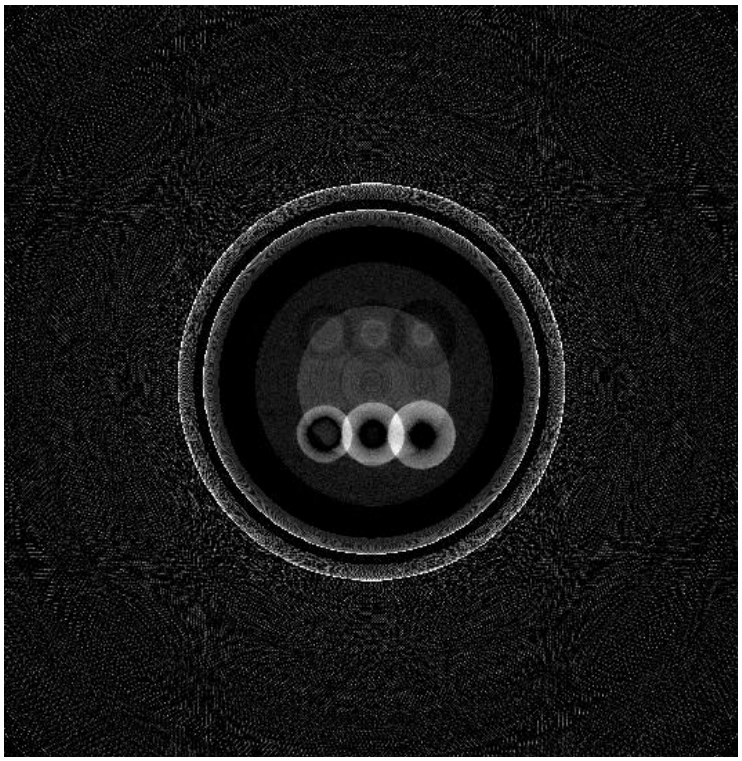

2-21. Reconstruction of the image before geometric optimization, detector linearization, or beam hardening correction.

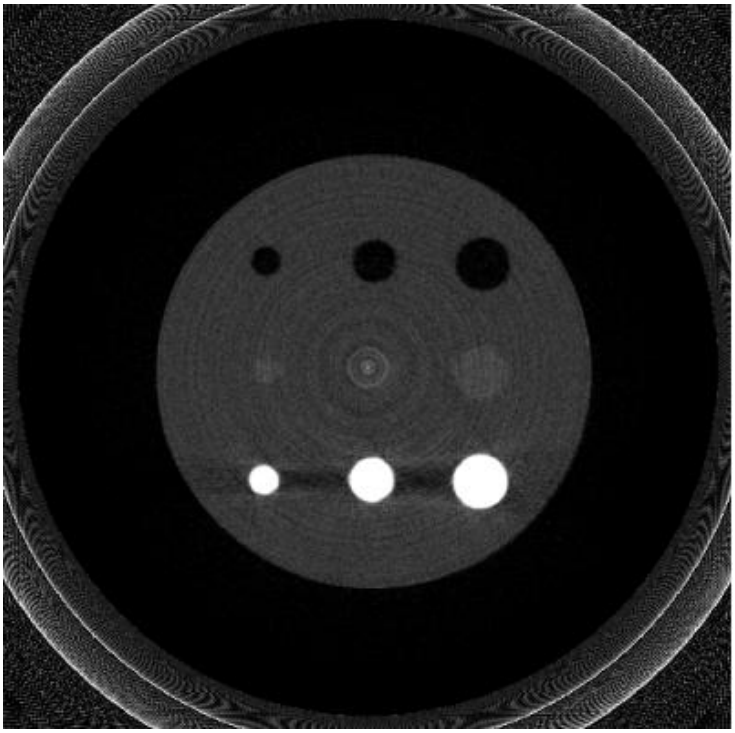

Figure 2-22. Reconstruction of the image after geometric parameter optimization only. Ring artifacts are still very visible as are the beam hardening streak artifacts between the denser (brighter) objects. The combined effect of the gap between detectors and detector edge can be seen as the band encircling the whole object.

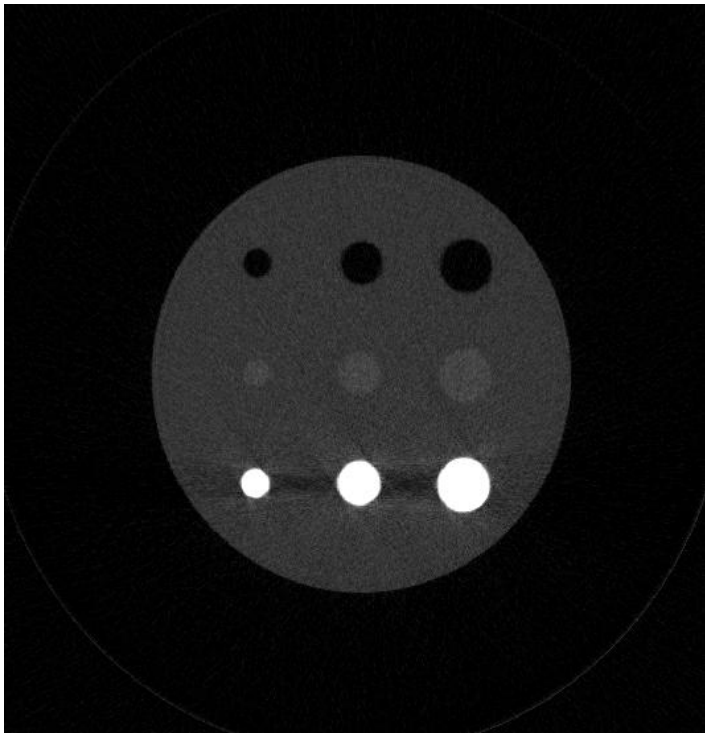

Figure 2-23. Reconstruction of the image after geometric parameter optimization and detector linearization. Effects of the detectors' gap were reduced by linear interpolation between the detectors. Beam hardening artifact's can still be seen.

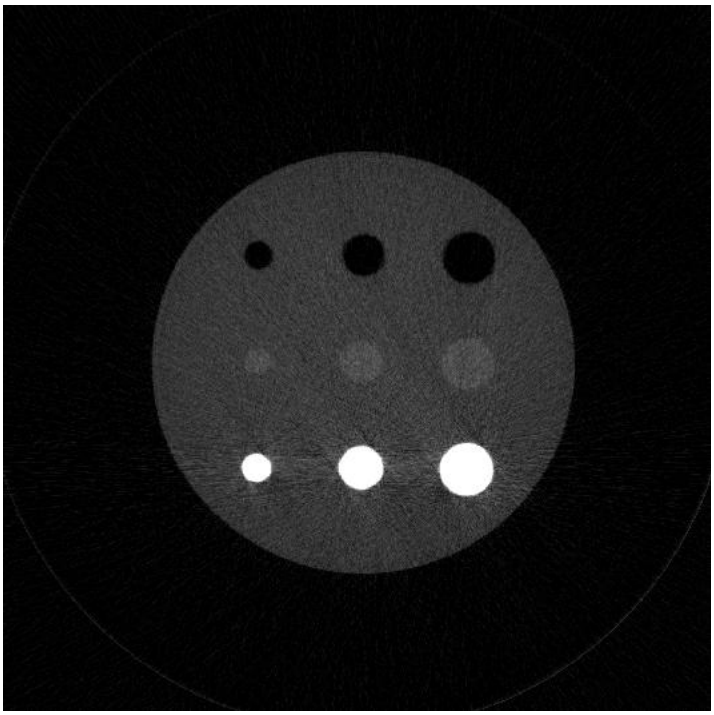

Figure 2-24. Result of reconstructed test phantom after full optimization (linearization of detector and beam hardening correction).

3. Correction for Patient Translational Motion

Patient motion during data acquisition in computed tomography scanners causes a decrease in the quality of an image known as motion artifact. This can lead to a decrease in resolution, and the detection of finer details could be missed. One of the more noticeable types of motion is translation motion. There are currently several known methods for correction of this motion in both parallel-beam and fan-beam CT, many of which require the patient to wear objects to record the motion data. Almost all of these methods include the use of the sinogram.

The sinogram represents perhaps the most sensitive data for determining the motion of the patient. These are the images of the projection data taken at each source position. The rotation of the source causes the image to appear as a series of several sinusoids of various intensities and widths. Figure 3-1 shows a reconstructed image and its sinogram.

In CT scanners, small, dense objects, called fiducial markers, are commonly used to track the patient motion [7, 8, 9]. These markers are superficially attached to the patient. In a sinogram image, these markers are easily identifiable due to their density. Variation of the markers from an ideal sinusoid represents motion data [8].

.

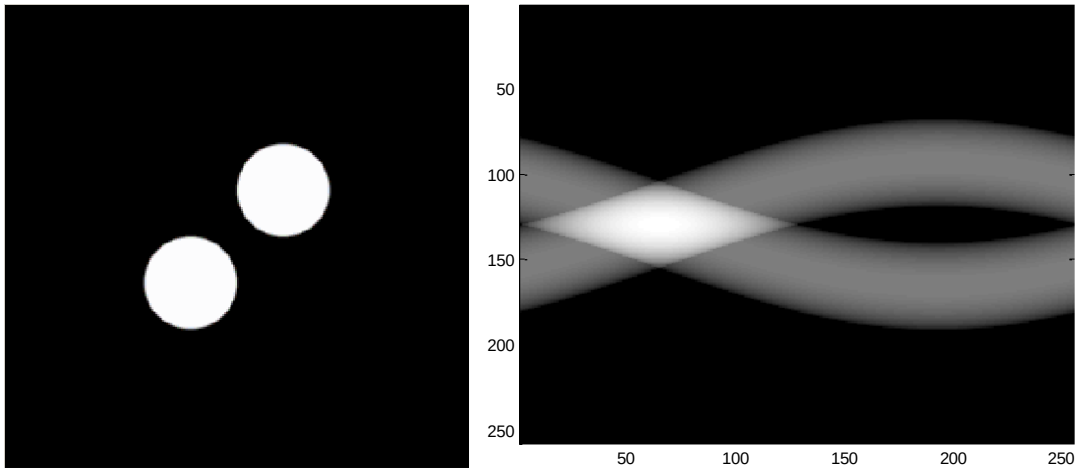

Figure 3-1. Original Image (left) and its sinogram (right) for a parallel-beam scanner. For the sinogram image, the vertical axis shows the data position of the projection for a detector with 250 elements, and the horizontal axis shows the source position evenly incremented 250 times over 360°.

For this experiment, a program was used to simulate the data of a 3rd generation fan-beam CT scanner with a flat detector and an equivalent distance for the source to the center-of-rotation and the center-of-rotation to the detector. In a fan-beam CT scanner, the sinogram image is slightly altered from perfect sinusoids by the geometry of the fan-beam itself.

Figure 3-2 shows the resulting geometry, where the position of the ray incident on detector p is given by the following trigonometric equations:

$$c^2 = b^2 + Ro^2 + 2 \cdot b \cdot Ro \cdot \cos\beta \tag{3.1}$$

$$\frac{c}{\sin\beta} = \frac{b}{\sin\gamma}, \tag{3.2}$$

where Ro is the distance from the source to the center-of-rotation, b is the distance from the center to the ray intersecting the x-axis, and β is the gantry angle of the source. Solving these equations for γ gives the angle between the midline that passes through the center-of-rotation and the ray.

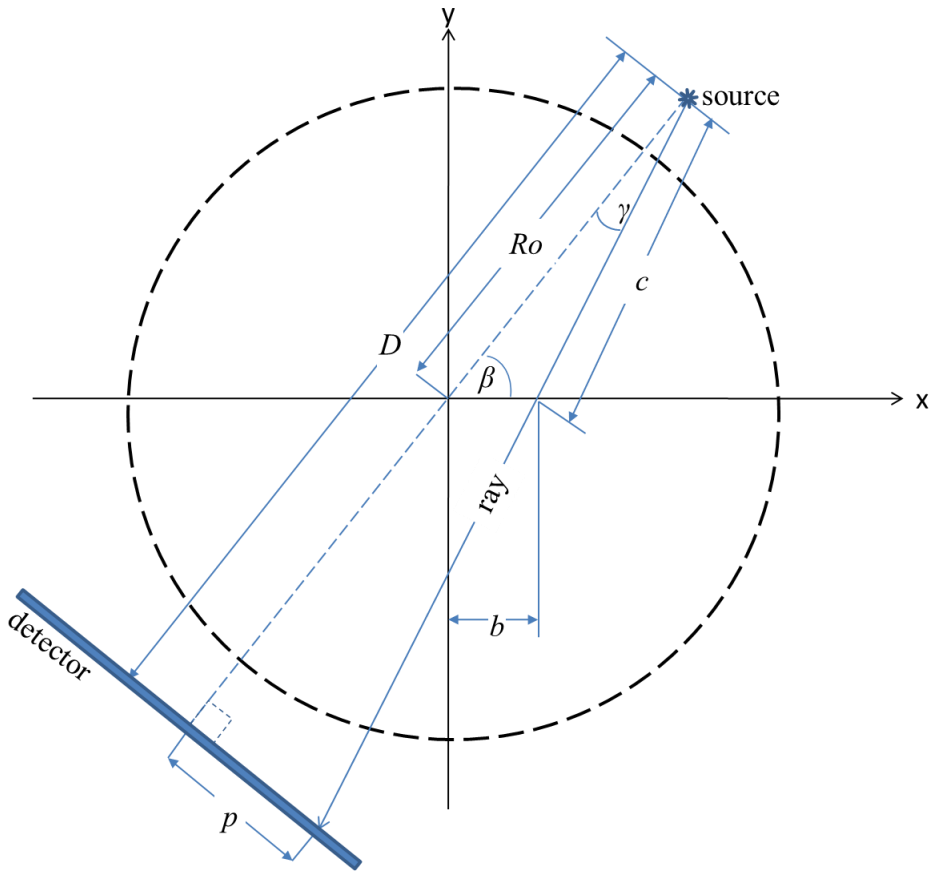

Figure 3-2. Geometry of a source ray incident on a detector for fan-beam CT

$$\gamma = \sin^{-1}\left(\frac{b \sin\beta}{c}\right) \tag{3.3}$$

Using simple, right-triangle geometry, the position p of the ray incident on the detector can be given by Equation 3.4.

$$p(\gamma) = D \tan\gamma \tag{3.4}$$

where D is source-to-detector distance along the midline that it passes through the center-of-rotation (shown as the dashed line in Figure 3-2). Using these results, we can see in

Figure 3-3 that the sinusoid-like curve used to create the sinogram images in fan-beam CT is slightly different compared to that of a true sinusoid used to create the sinogram images in parallel-beam CT. In the sinogram images themselves, these differences are not readily noticeable. However, the mathematical differences do affect the calculations of the center of mass of the objects.

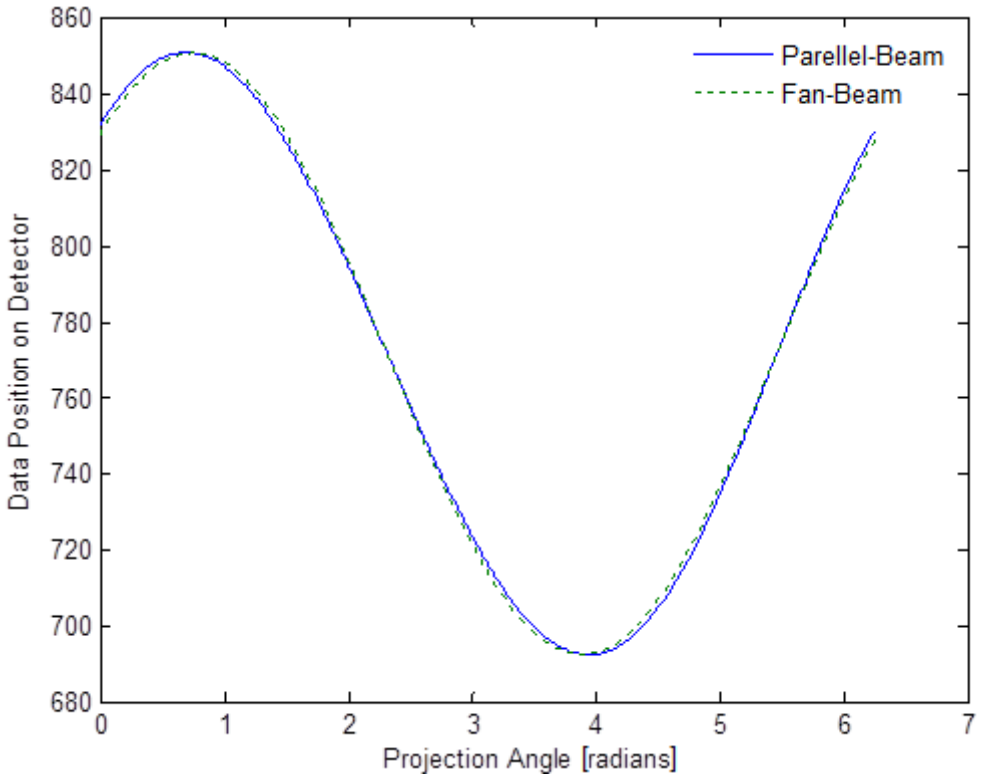

Figure 3-3. Variation in position of a single point between parallel-beam and fan-beam.

Another difference between parallel-beam CT and fan-beam CT caused by this geometry is the integral curve seen as the sum of the intensities in the projections versus the source angle of the projection. For a parallel-beam CT scanner, the plot of the sum of intensities at each projection angle of an uncorrupted image would be seen as a straight line parallel to the x-axis, as the definite integral is constant at each angle of projection. However, for a fan-beam CT scanner, a motion-free plot of this should be seen as a perfect sinusoid.

Additional information about the translation-motion of an object can be derived from this sinusoid that would not be available from a plot for parallel-beam CT. This is because the distance between the source and the object will affect the number of source rays that pass through the object on their path to the detector (i.e., magnification).

3.1 Methods for Translational Motion Correction

3.1.1 Determination of Ideal Data for the Definite Integral and the Center of Mass of the Sinogram.

To begin the correction for translation in the sinogram, the sum of the intensities was calculated at each projection from the sinogram and then plotted against the angle of that projection. For matrices with a small number of pixels, the resolution was increased by resizing the individual projections of the image through bi-linear interpolation. This created more data for a smoother calculation of the ideal integral and center of mass

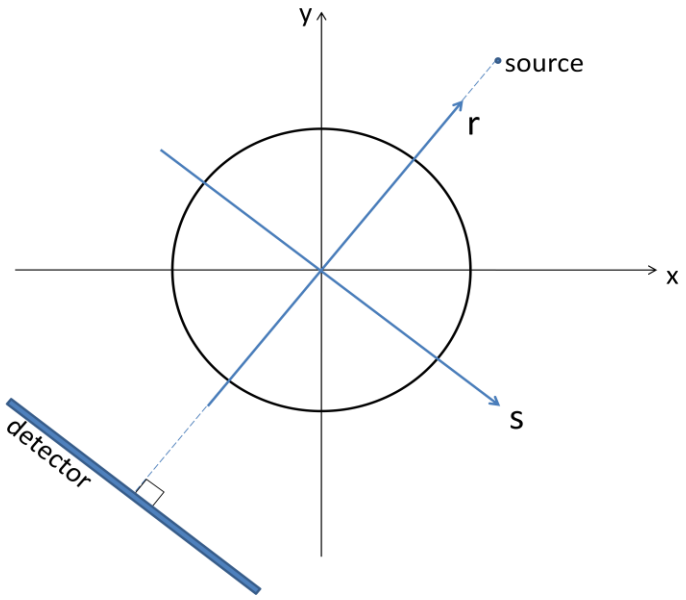

Figure 3-4. Rotating frame of reference, where r is equivalent to y and s is equivalent to x at the initial source position $\beta=0^{o}$.

sinusoids. This plot gives information about the translational motion of the object parallel to the r-axis in the rotating frame of reference seen in Figure 3-4. When compared to the ideal sinusoid, the definite integral will either increase as the object moves toward the source or decrease as it moves away from the source (i.e., increasing or decreasing magnification of the projection). Figure 3-5 shows a sample motion-encoded curve of projection integrals due to translational motion and the ideal curve for these data.

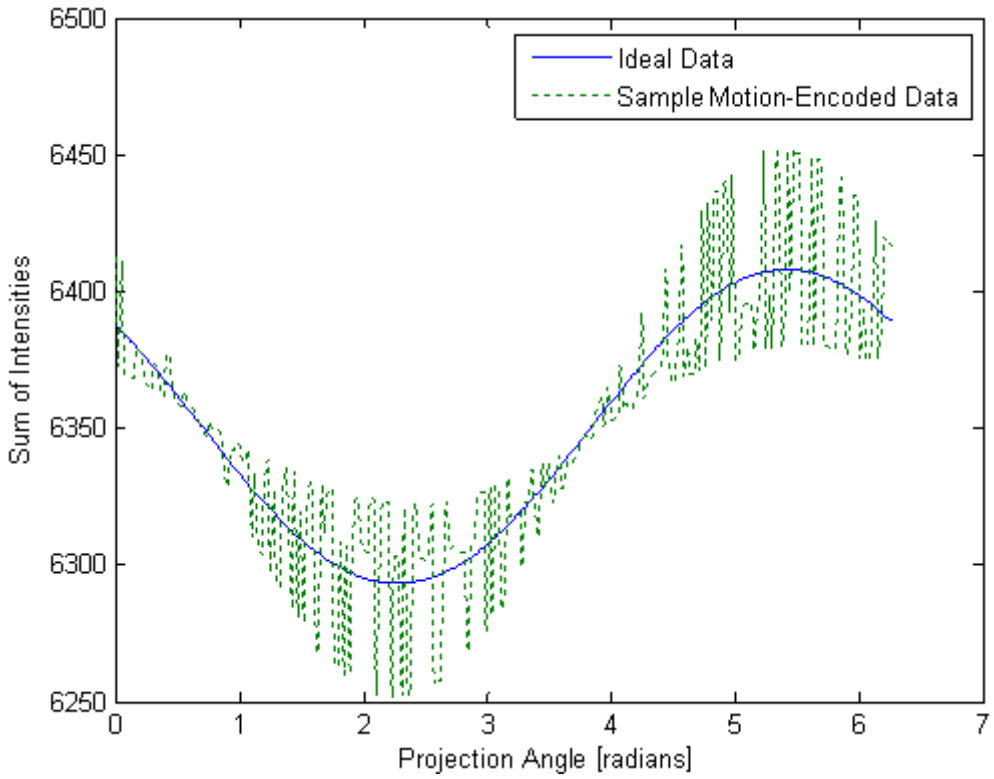

Figure 3-5: Typical motion-encoded data from an object in translational motion and the ideal sinusoid for the definite integral at each projection angle in radians. Each peak in the motion-encoded data represents a motion increment.

The ideal sinusoidal curve was determined by applying the Fourier transform to the motion-encoded data. By using the magnitude of the coefficient C_0 as the DC value and the complex coefficient C_1 for the amplitude and phase angle, the ideal sinusoid was found using the formula

$$f(\beta) = |C_0| + |C_1|cos(\beta + \varphi), \tag{3.5}$$

where β is the source angle and φ is the phase angle.

Similar to the integral sinusoid, the center of mass of the projection at each angle also provides useful information about the motion of the object. The ideal plot of the center of mass as a function of the source angle also follows the basic form of a sinusoid. The center of mass curves of an ideal and a motion-encoded sinogram are shown in Figure 3-6.

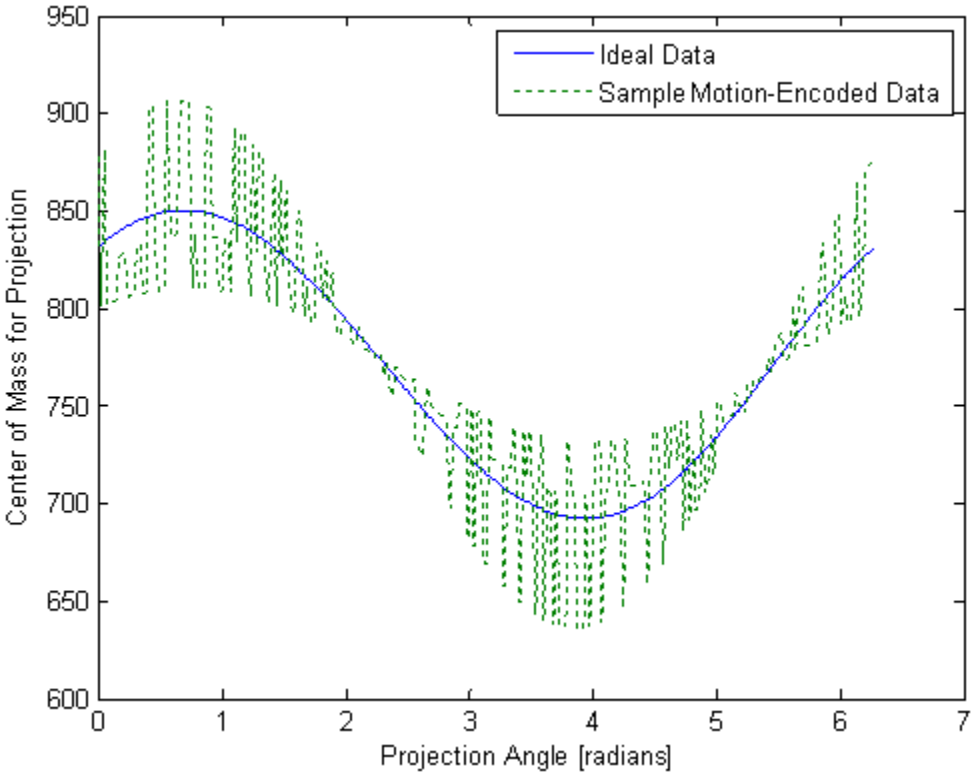

Figure 3-6. Motion-encoded data from an object in translation motion and the ideal curve for the center of mass vs. projection angle in radians. The simulated motion is from the same projection data used for Figure 3-5.

The ideal sinusoid for the center of mass was determined similarly to the ideal sinusoid for the integral. A Fourier transform was applied to the data. The detector element E was used instead of the magnitude of the coefficient C_0 for the DC value. The complex

coefficient C_1 was still used for the amplitude and phase angle of the ideal sinusoid. Equation 3.5 was used again to determine the best fit of a sinusoidal curve. However, the center of mass sinusoid was altered slightly as shown in Equations 3.1 through 3.4 because of the fan-angle compared to the angle of the source. In the general case for a known centroid position of an object, Equation 2.1 (restated below for convenience) can be used to estimate the center of mass curve by assuming the center of mass is a single point at location (x_o, y_o).

$$p(\beta) = D(x_o \cos\beta + y_o \sin\beta - \tau)/(x_o \sin\beta - y_o \sin\beta + Ro) + c \qquad (2.1)$$

The position of (x_o, y_o) can be estimated by first calculating the maximum distance of $f(\beta)$ from C_o to determine r (the distance in polar coordinates). Figure 3-7 shows how the object space relates to the sinogram for a parallel-beam scan. With the small field of view for the fHRCT, a reasonable approximation for (x_o, y_o) can be obtained after first adjusting for the effect of the fan-beam magnification. Multiplying r by the ratio Ro/D helps adjust for this magnification before the final calculation of x_o and y_o(Equation 3.6).

$$r' = r \times Ro/D \qquad (3.6)$$

Using this distance in conjunction with the phase angle from C_1 (φ) to employ a polar-to-Cartesian coordinate conversion, an approximation of (x_o, y_o) can be calculated; $x_o = r' \times cos\varphi$ and $y_o = r' \times sin\varphi$. By inserting these values into Equation 2.1, a reasonable estimation of the ideal curve for the center of mass for an offset midline is given. By comparing the motion-encoded data with the ideal data for the center of mass, motion parallel to the s-axis in the rotating frame of reference can clearly be shown.

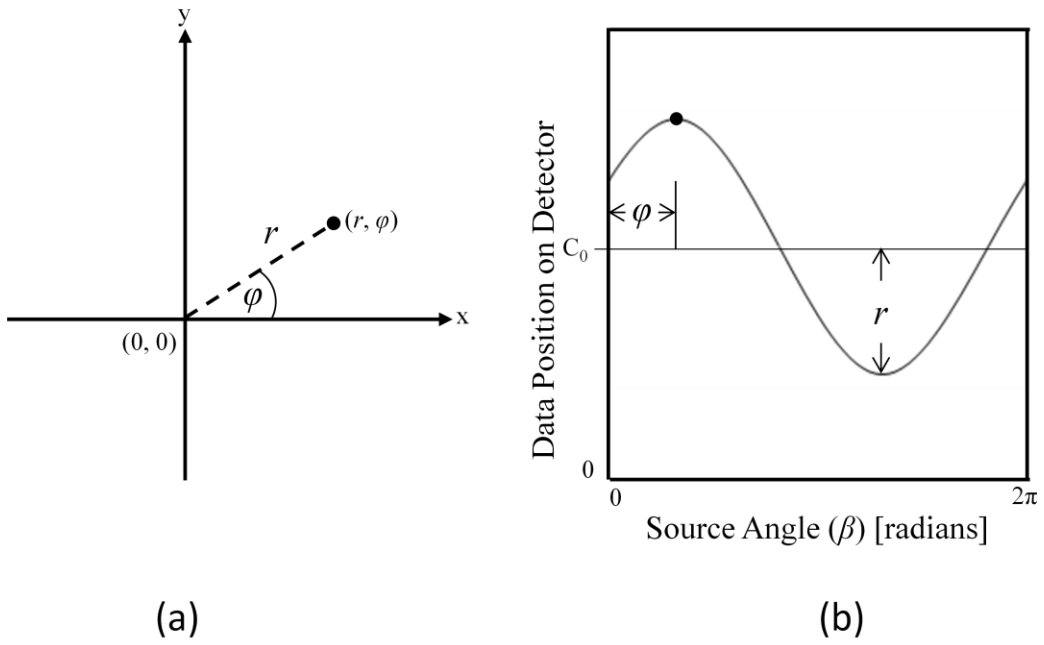

Figure 3-7. The relationship between (a) a single point located in the object space (i.e., xy coordinate plane) and (b) the same point in the sinogram space from $0 \leq \beta \leq 2\pi$ (adapted from [10]).

3.1.2 Correction of Sinogram Image

Once the ideal sinusoids are estimated, the measured sinogram data can be corrected projection by projection. For each projection, the positions of the projection data in the sinogram matrix are adjusted based on the increase or decrease in magnification determined from the ratio of the integral calculated from the motion-encoded sinogram to the ideal integral determined from the FFT. The positions are adjusted by expanding or compressing the distances of the individual projection points relative to the center data point of the projection data by a factor inverse to the ratio calculated. Therefore, a ratio greater than 1 suggests magnification of the projection, and steps are taken to reverse this magnification by converging the pixels toward the center pixel by a factor less than 1.

After correcting for magnification, each projection is then shifted up or down in the sinogram matrix based on the differences between the actual center of mass and the calculated ideal center of mass. Once this is done, the sinogram image is resized to its original resolution using bi-linear interpolation if necessary.

3.2 Method for Determining Error between Motion-Free and Motion-Corrected Images

Once the sinogram matrix is processed for translation motion correction using the procedures above, the image is reconstructed using filtered back projection. The quantitative comparison was made by determining the fractional difference between the original, motion-free image and the motion-corrected image, i.e., by calculating the sum of the absolute differences at each pixel between the motion-free and the motion-corrected image and dividing by the sum of the intensity value of the pixels for the motion-free image. This was done after each image was processed by removing the background image and aligning the images so that the smallest percent difference was found.

For the images created from the simulation program, the background of each image was removed so that pixel values of the reconstructed backgrounds would not influence the results for the important parts of the object. This was done by applying to each image, the motion-free and the motion-corrected image, an individual mask. The masks where created individually for each simulated image using the following procedure. First, the Sobel method for edge finding was applied to the image. This method allows for good results in finding the edges of the object in the reconstructed image at all angles. The edge lines were then turned into a binary gradient mask. This binary gradient mask was

then dilated three times, and holes between the edge lines were filled. The mask was then eroded three times to obtain a mask of the original size. Each of the final masks were multiplied with the respective reconstructed image to remove the background.

For the experimentally measured images, the mask was created using a simple threshold to create a binary image. Edge finding was not as practical in the experimental image reconstructions because the gradients between the edges and the background were lower. Any holes were filled as described above using the procedure of a single opening, followed by filling, and then five dilations of the binary mask. This created a mask that was slightly larger than the object to insure that the relevant structures in the experimental images were preserved despite the lack of edge-finding techniques.

Once the background was removed, the images needed to be aligned. Alignment is necessary because the object in the motion-corrected image may not have been in the same position as the object in the motion-free image. This was done by shifting the motion-corrected image matrix up and down and calculating the difference from the motion-free image matrix at each shift. The motion-corrected image matrix was then set to the shifted position with the lowest difference. This process was repeated by shifting the motion-corrected image matrix left and right to find the minimum difference between the two image matrices. Additional up/down and left right shifts eventually led to optimally aligned images. In our case, a total of three iterations of up/down and left right shift pairs were sufficient.

3.3 Results

For the quantitative and qualitative analysis, the simulated object shown in Figure 3-8 was used. This figure consists of a 2.7 cm diameter reconstruction area. The source-detector assembly was rotated 360 degrees with 500 evenly spaced source positions and a detector size of 1024 elements. The uncorrupted sinogram image of the projections is shown in Figure 3-9.

3.3.1 Qualitative Analysis

Simulated and experimental results were obtained to qualitatively observe the effectiveness of the motion-correction method.

3.3.1.1 Simulated Qualitative Analysis

Figure 3-10 shows the motion-encoded sinogram image due to translational motion of the object throughout the scan. This included negative x and negative y-direction motions with distances ranging from 0 to 5 mm from the center at random times from the start of the scan. The reconstructed image from this sinogram is shown in Figure 3-11. The object is barely recognizable due to the large amount of motion. After applying the translational motion correction method described earlier to the motion-encoded sinogram (Figure 3-10), a much smoother sinogram results (Figure 3-12). It can be seen that sinograms in Figures 3-9 and 3-12 have substantially smoother transitions than the motion-encoded sinogram seen in Figure 3-10.

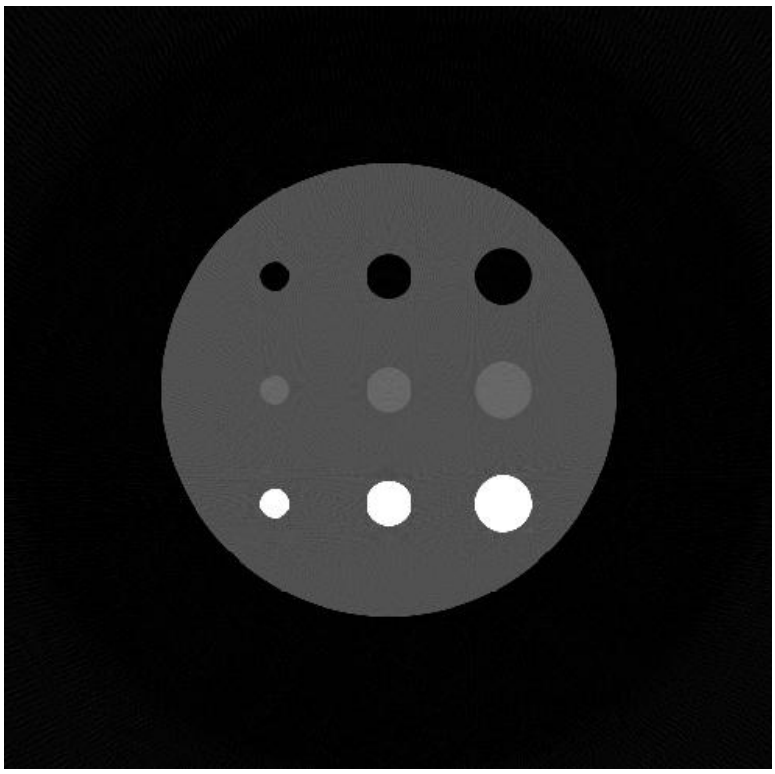

Figure 3-8. Reconstruction of the simulated image, uncorrupted by motion.

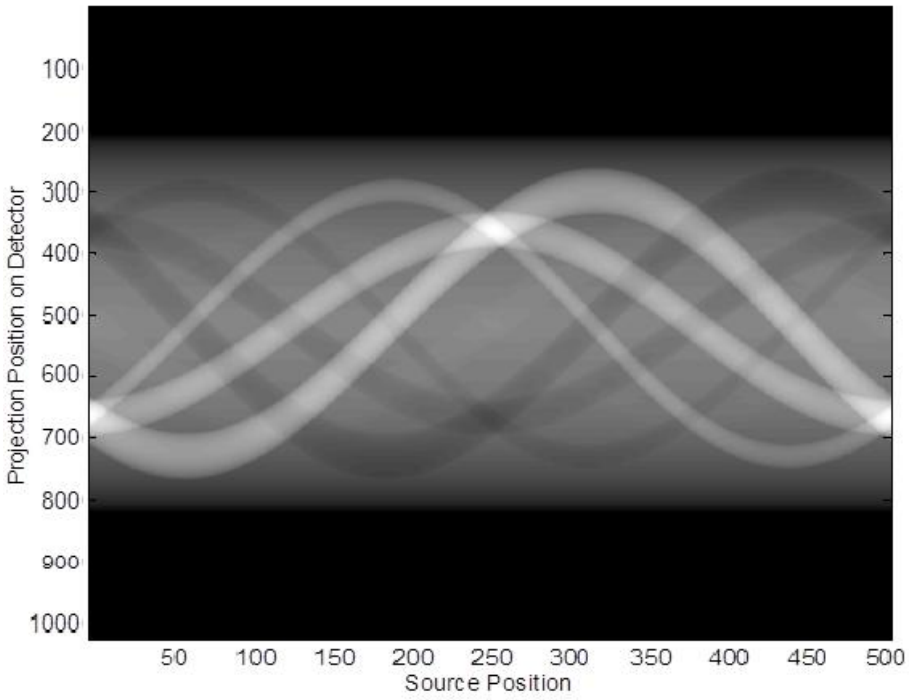

Figure 3-9. Simulation of the motion-free sinogram of the projections for the object shown in Figure 3-8.

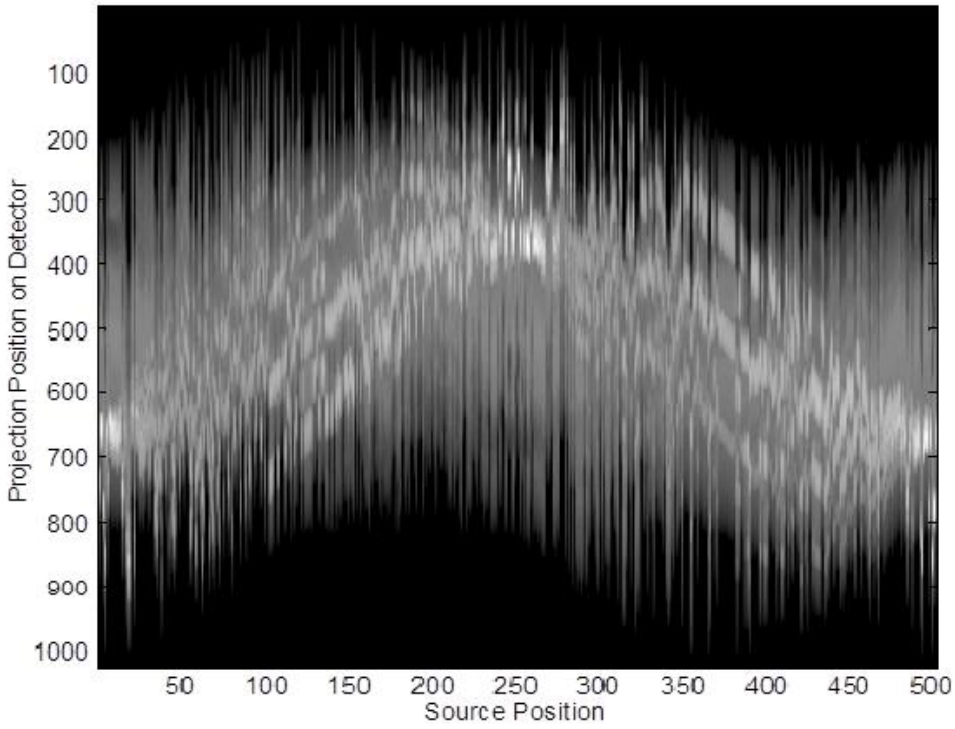

Figure 3-10. Simulated motion-encoded sinogram image due to translational motion of the object during the scan. The motion-encoded sinogram contains a randomly assigned projection at each source position from 11 different sinograms obtained from 11 different translation positions with up to 5 mm offset.

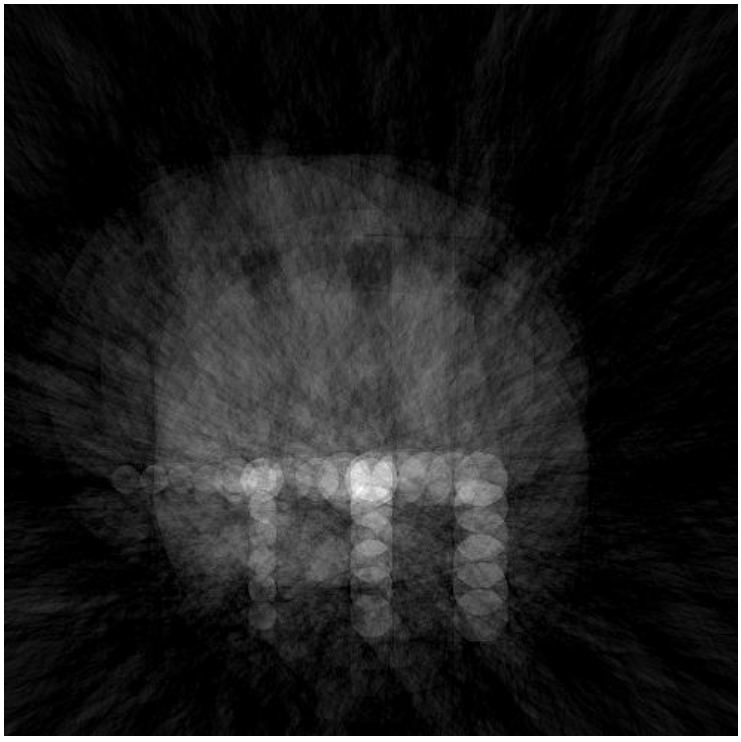

Figure 3-11. Reconstructed image of the simulated motion-encoded sinogram matrix (Figure 3-10).

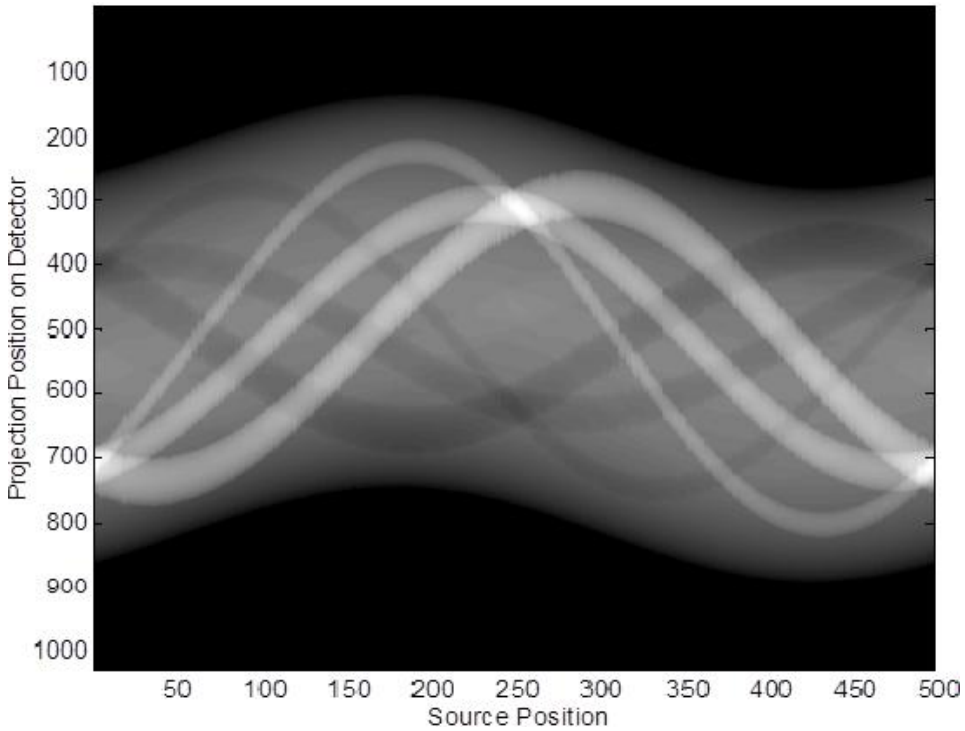

Figure 3-12. Sinogram image after applying the translational motion correction method to the sinogram shown in Figure 3-10.

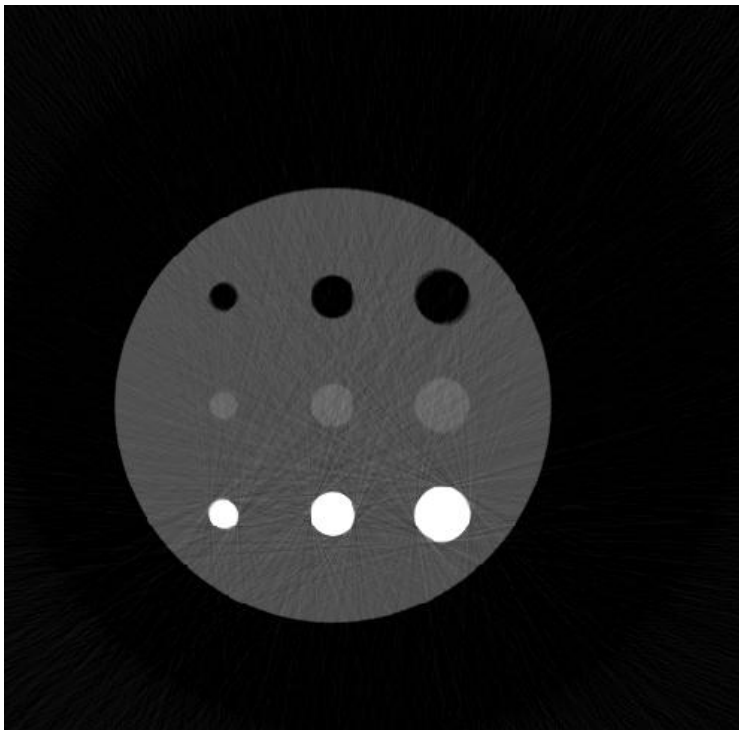

Figure 3-13. Simulated motion-corrected reconstructed image of the motion-corrected sinogram matrix.

The reconstructed image from the motion-corrected sinogram matrix (Figure 3-12) can be seen in Figure 3-13. The object is well recognizable and shows qualitatively little difference to the original image (Figure 3-8). There are, however, small differences in the boundaries, highlighted by subtracting the two images from each other (Figure 3-14).

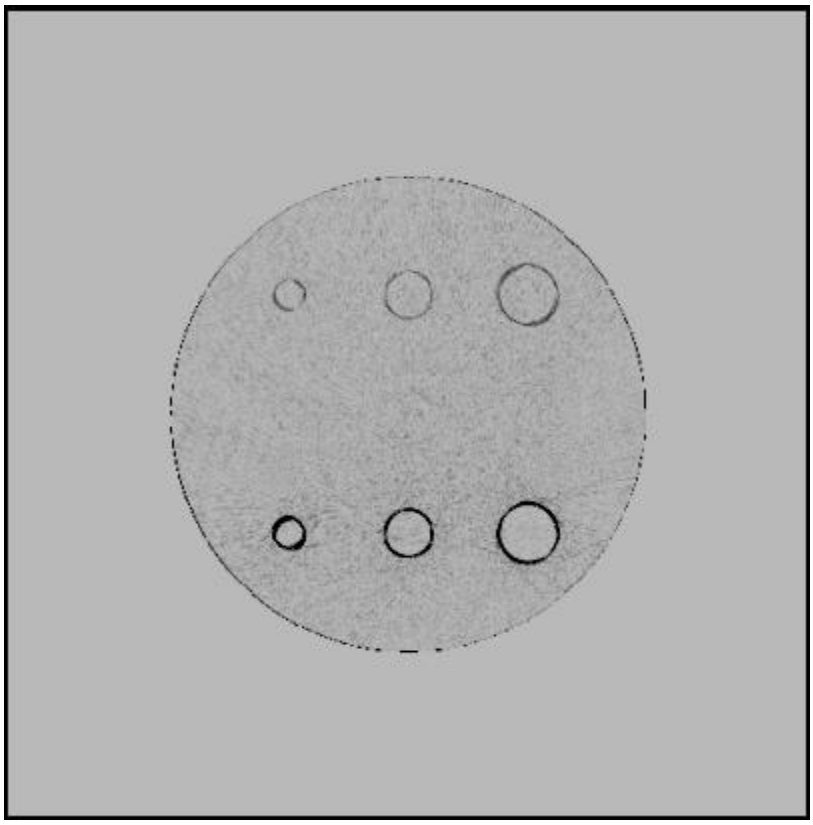

Figure 3-14. Visual representation of the point-by-point absolute value differences between the simulated reconstructed motion-free and motion-corrected images (Figures 3-8 and 3-12, respectively). The image has been inverted and contrast/brightness was adjusted to further highlight the differences.

3.3.1.2 Experimental Qualitative Analysis

For the simulation analysis in the previous section, an object was created that closely reproduced the characteristics (e.g. dimensions, densities, etc.) of the experimental phantom (reconstruction shown in section 2.4, Figure 2-24). The sinogram of the experimental phantom positioned at the center-of-rotation can be seen in Figure 3-15.

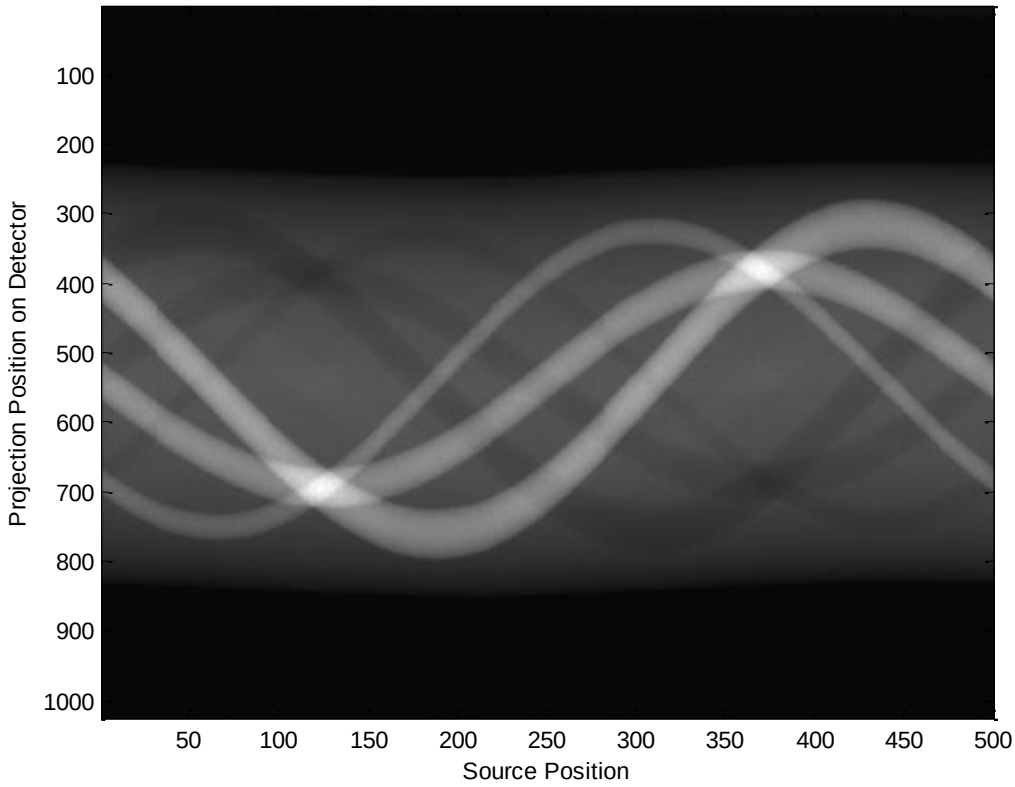

Figure 3-15. Motion-free sinogram of the experiment phantom shown in Figure 2-24.

The motion produced for the experimental data was structured specifically to study the different types of translational motion (e.g. x-axis and y-axis motion). Figure 3-16 is an example of a sinogram created from profiles of two full, experimental scans, one with a 4 mm offset, and combining profiles from each to simulate a 4 mm motion initially along the r-axis toward the source (i.e. sinogram of the 4 mm offset along the negative x-axis at $90^{o} \leq \beta < 270^{o}$).

The reconstruction of the uncorrected sinogram shows the amount of motion between the initial position and the offset position. The 4 mm offset is nearly 25% of the diameter of the large, outermost disk of the experimental phantom.

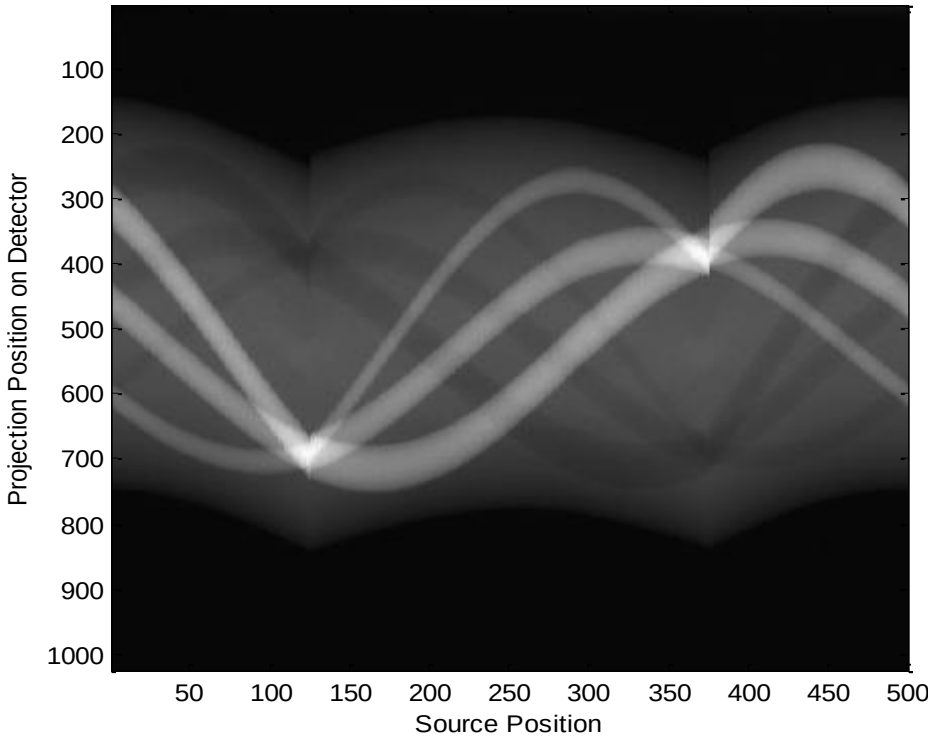

Figure 3-16. Motion-encoded sinogram simulating abrupt r-axis motion at $\beta = 90^{o}$.

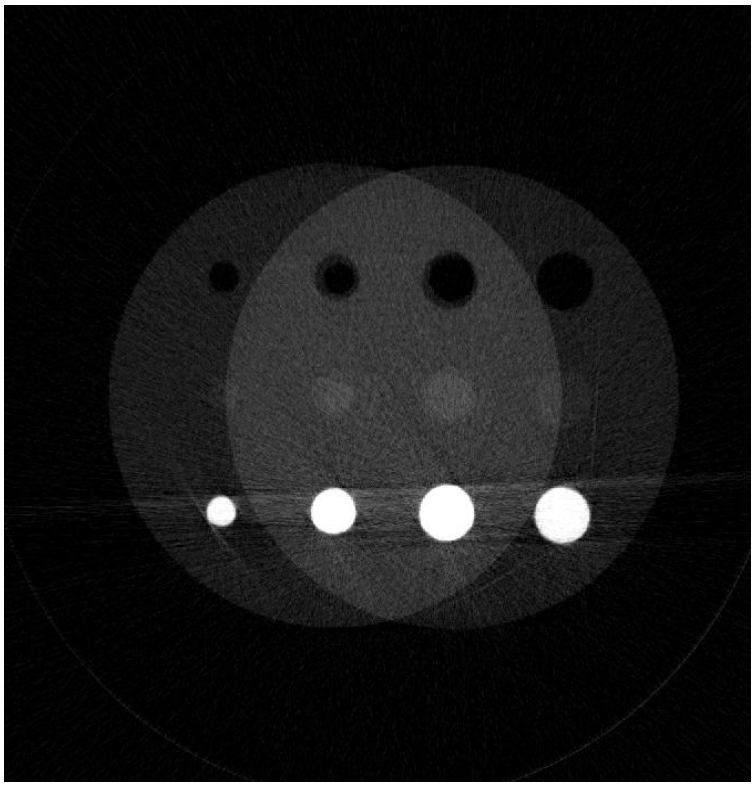

Figure 3-17. Reconstructed image of the motion-encoded sinogram (Figure 3-16).

The motion-encoded sinogram was then subjected to the motion-correction method, the result of which is shown in Figure 3-18. The reconstructed image of this corrected sinogram is shown in Figure 3-19. Again, the image is recognizable. Though small qualitative differences are apparent, it is hard to discern any large differences between the motion-free and the motion-corrected images. The most noticeable effects from the motion-correction can be seen near the structure edges. These effects are highlighted in Figure 3-20.

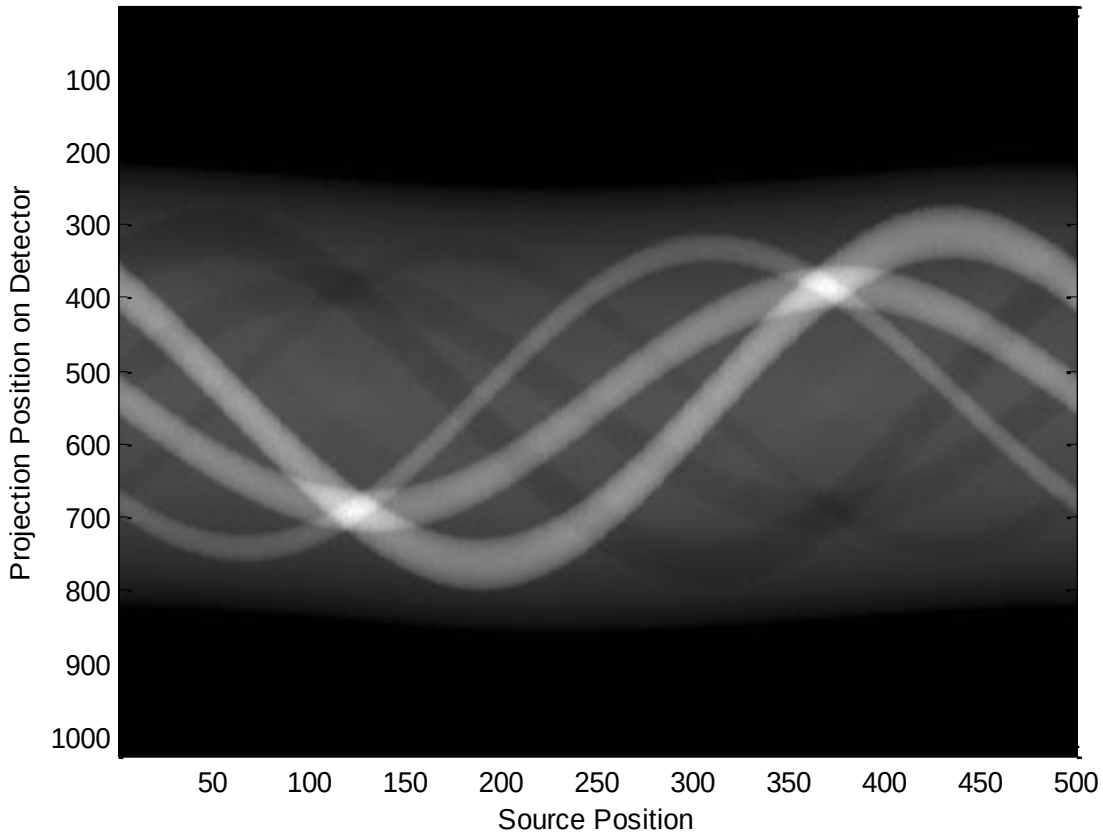

Figure 3-18. Motion-corrected sinogram of the motion-encoded sinogram (Figure 3-16).

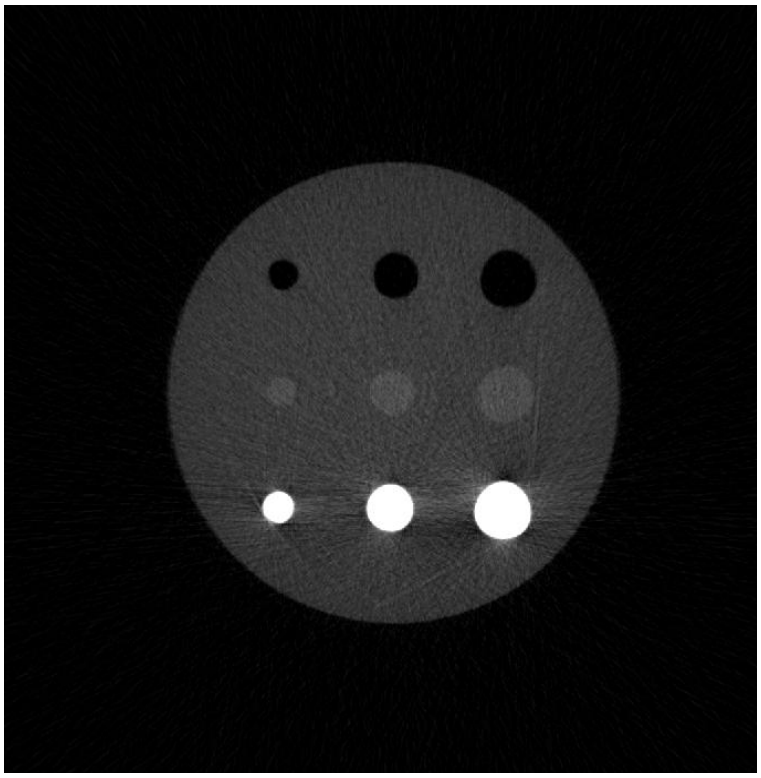

Figure 3-19. Reconstructed image of the motion-corrected sinogram (Figure 3-18).

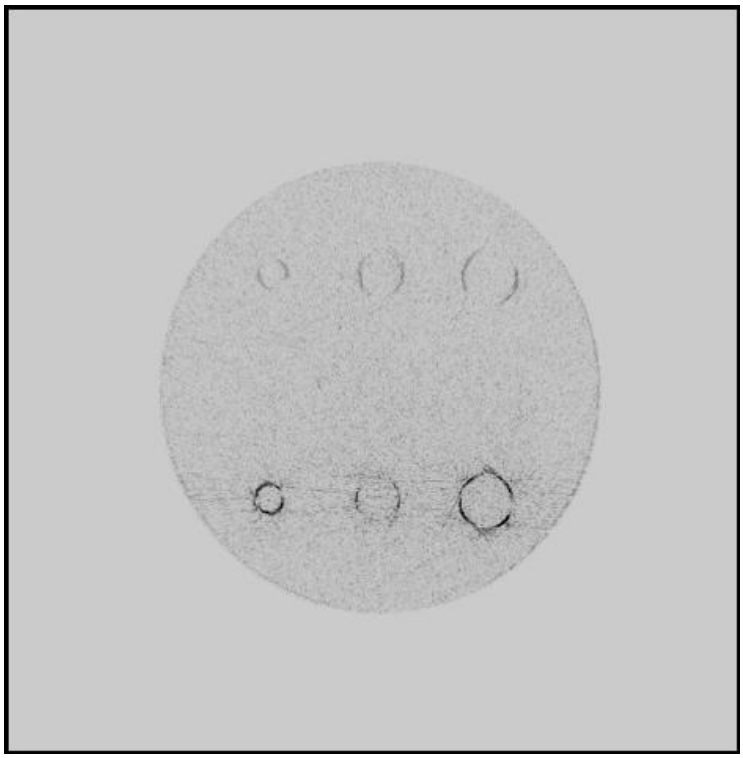

Figure 3-20. Visual representation of the point-by-point absolute value differences between the experimental reconstructed motion-free and motion-corrected images (Figures 2-24 and 3-19, respectively). The image has been inverted, and contrast/brightness was adjusted to further highlight the differences.

For qualitative comparison, the angle of the 4 mm offset was initiated so that the breaks in the sinogram occurred along the s-axis direction. Figure 3-21 is an example of a sinogram created, using the same process as for Figure 3-16, to simulate a 4 mm motion initially along the negative s-axis (i.e. 4 mm motion in the negative x-axis direction at $180^{o} \leq \beta < 360^{o}$).

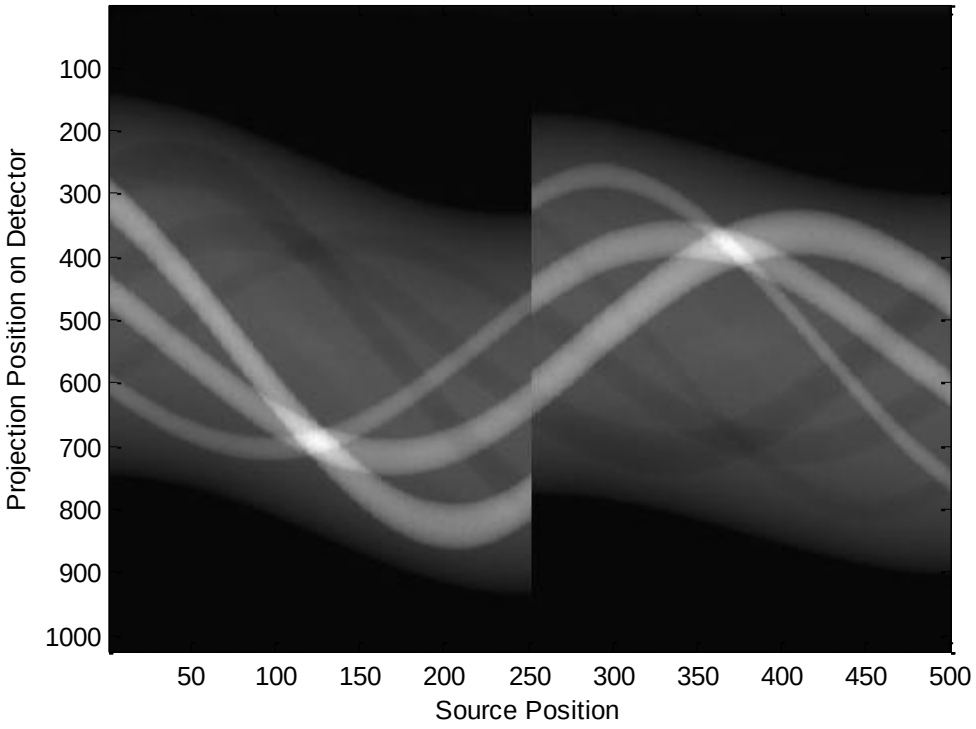

Figure 3-21. Motion-encoded sinogram of experimental data simulating abrupt s-axis motion at $\beta = 180^{o}$ using experimental data.

The motion-encoded sinogram was again subjected to the motion-correction reduction method, resulting in Figure 3-23. The reconstructed image is shown in Figure 3-24. Residual effects of the motion after motion-correction are more apparent in Figure 3-24 than in Figure 3-19, despite the same distance and duration of the offset motion. The

differences between the uncorrupted and the motion-corrected images (Figures 2-24 and 3-24, respectively) are again highlighted in Figure 3-25.

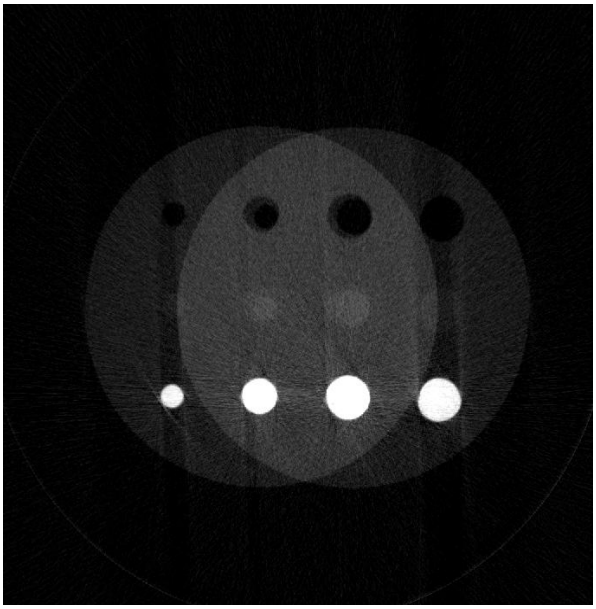

Figure 3-22. Reconstructed image of the simulated motion-encoded sinogram matrix (Figure 3-21).

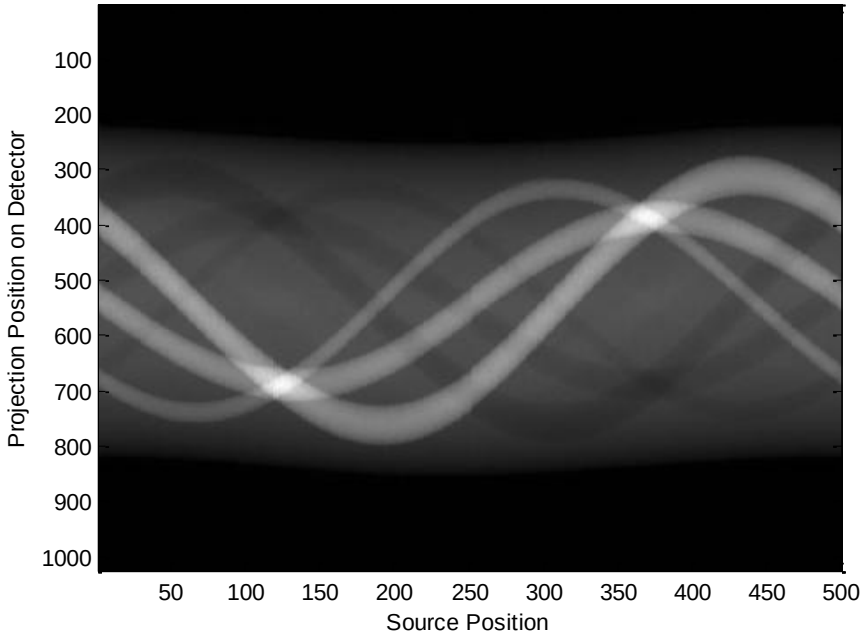

Figure 3-23. Sinogram image after applying the translational motion-correction method to the sinogram (Figure 3-21).

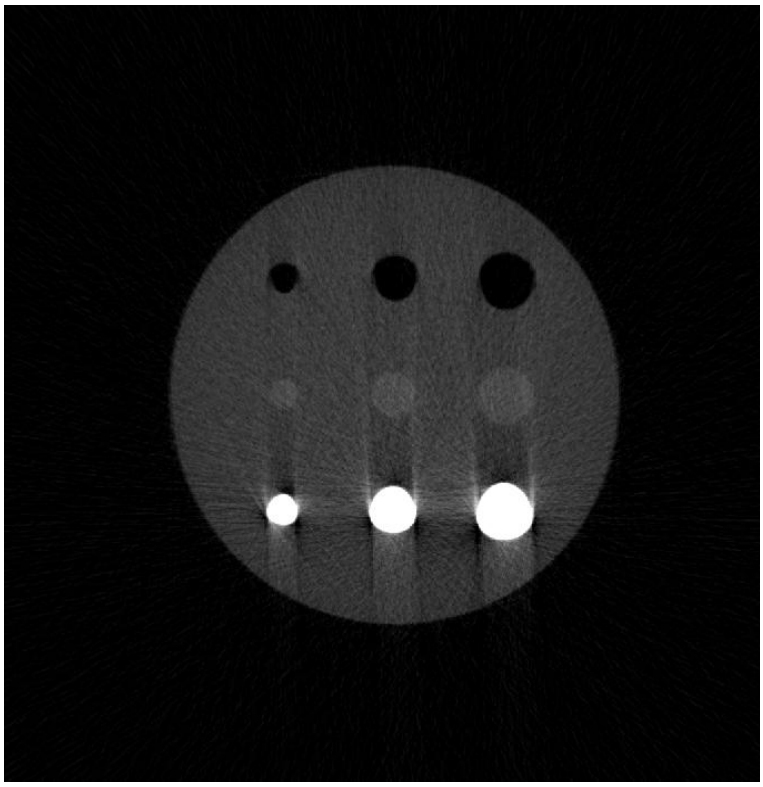

Figure 3-24. Simulated motion-corrected reconstructed image of the motion-corrected sinogram matrix (Figure 3-23).

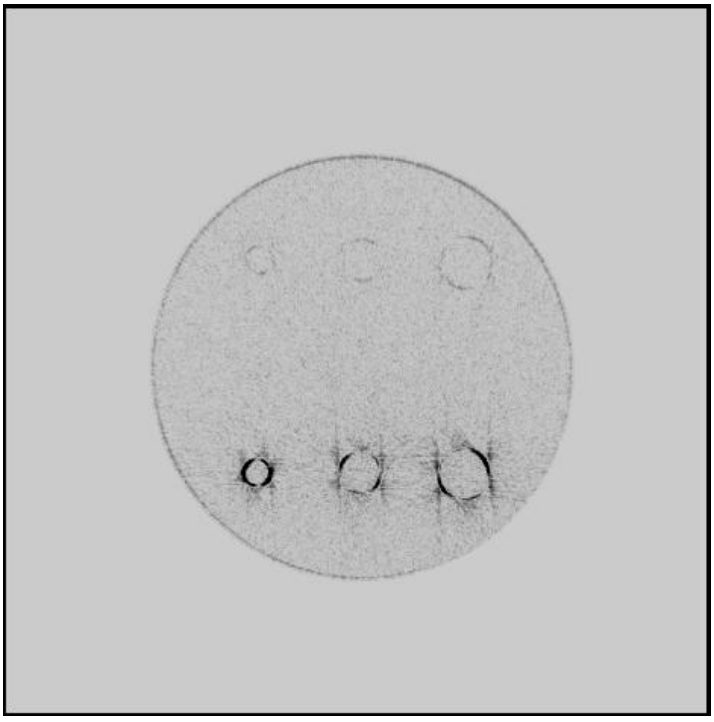

Figure 3-25. Visual representation of the point-by-point absolute value differences between the experimental reconstructed motion-free and motion-corrected images (Figures 2-24 and 3-24, respectively). The difference image has been inverted.

3.3.2 Quantitative Analysis

The percent error between the motion-corrected image in Figure 3-13 and the original image Figure 3-8 was calculated to determine the quantitative difference between them. This was determined by using the sum of the absolute values of the differences in image values and dividing by the sum of the intensities in the uncorrupted image. A value of 0.198 (19.8%) was calculated as the difference between the two images compared to a value of 0.707 (70.7%) for the uncorrected image (Figure 3-11) to the image in Figure 3-8. These values include the effect of the background, as the amount of motion in Figure 3-11 was not easily masked. The rest of the analysis was done using the masked images as described earlier, giving the fractional value of 0.0678 (6.78%) as the overall difference between the motion-corrected image (Figure 3-13) and the original image (Figure 3-8).

Generally speaking, a true baseline value for the quantitative error is difficult to determine, as even a motion-free reconstructed image at position A will rarely be a 100% match with another motion-free reconstructed-image at position B given that A $\neq$ B. Figure 3-26 is a graph that illustrates the differences between motion-free images of the object at various offset distances for both the simulated and experimental scanner data. The average error was taken to be the mean of the errors where the offset $\neq$ 0 mm. It can be seen that the experimental data have a higher error than the simulated data. Some causes of the higher error include: more background is included in the error calculation due to the slightly larger mask for the experimental images, variation of the amount of photons that are incident on the detector due to noise, inaccuracies in the scanner

optimization, etc. This should be apparent given that even the experimental reconstructions at the same position (i.e., offset = 0) have an error of 0.0743(7.43%), as opposed to an error of 0% for the simulated results. The averages of these errors are 0.0515 with a standard deviation of 0.0040 and 0.1599 with a standard deviation of 0.0017 for the simulated and experimental data, respectively.

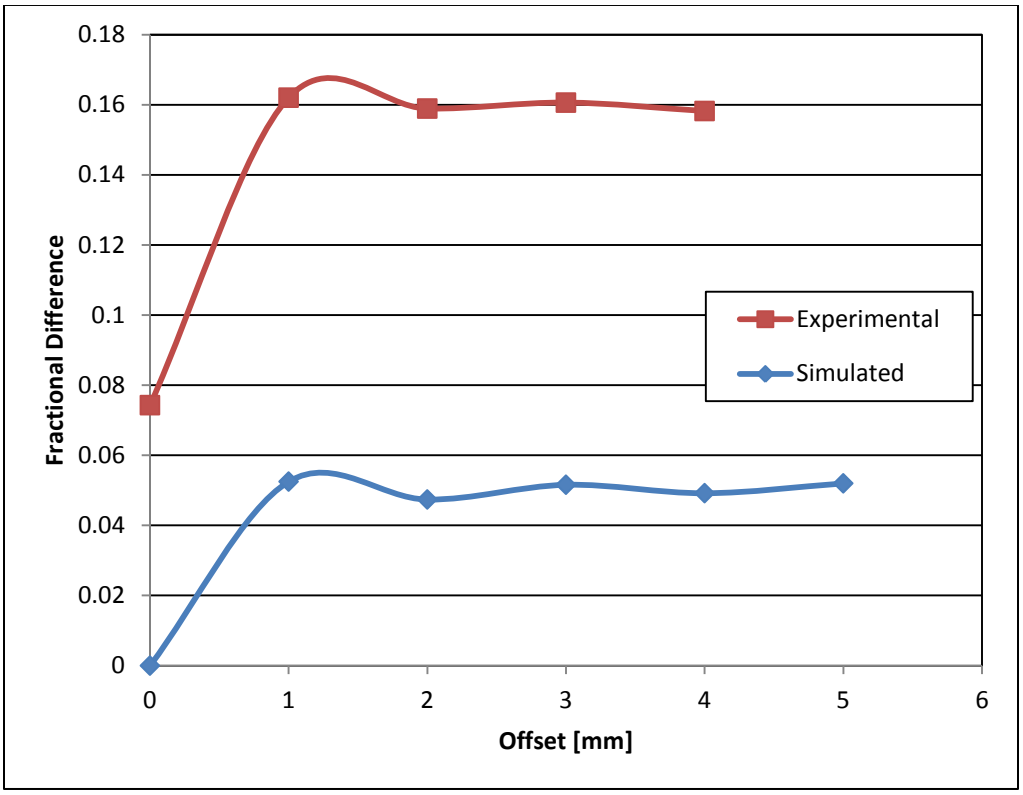

Figure 3-26. Differences of motion-free images of the object at various offset distances for both the simulated and experimental scanner data.

Aside from a random reassembly of sinograms taken from the object at varying translation positions, a more meticulous method was used to show the effects of the motion-correction method on the quality of the image. The various sets of motion-encoded sinograms include the distance of offset, angle at which the offset occurred, and the ratio of the sinograms involved. Figure 3-27 shows an example of a sinogram assembled from segments of two sinograms at differing positions to simulate a x-axis

motion from $0^o \leq \beta < 180^o$. The motion starts as an abrupt s-axis motion and transitions to a primarily r-axis motion back to an s-axis motion as the object maintains its position in the x-axis offset for 180^o.

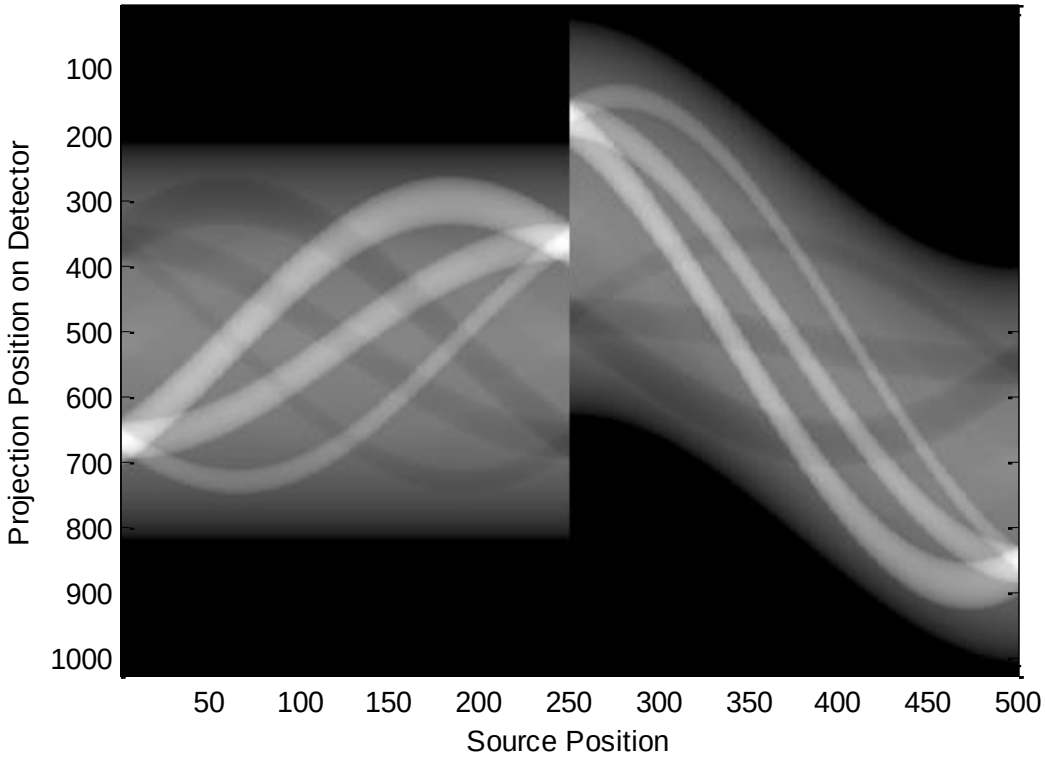

Figure 3-27. Construction of a sinogram to simulate motion using segments of 2 sinograms.

To study the effect of the offset distance on the motion-correction algorithm, we combined 50% of the sinogram for the object used as the relative starting position (i.e., 0 mm offset) with 50% of the sinogram for the object at offset distances of 1 mm - 4 mm for the experimental data and 1 mm - 5 mm for the simulated data. The sinograms were reassembled consistently, utilizing profiles from two scans, such that the motion simulated by an offset causes a continuity break primarily in the s-axis (i.e. parallel to the plane of the detector) and ended after 180^o rotation. If we assume the source position at $\beta = 0^o$ to be at the top of the positive y-axis (Refer to Figure 3-4), and the motion in the xy-

coordinate plane to be along the x-axis, then the replacement of 250 offset projections can occur from either $0^o \leq \beta < 180^o$ or $180^o \leq \beta < 360^o$. Figure 3-27 is an example of the construction of the motion-encoded sinogram for the latter. Figure 3-28 shows the results as fractional differences due to increasing distance of the object from the initial position for 50% of the sinogram. Figure 3-27 was corrected for motion and corresponds to the 5 mm offset for the simulated case in Figure 3-28. Figure 3-21 shows the experimental sinogram that was motion corrected and corresponds to the 4 mm offset in Figure 3-28.

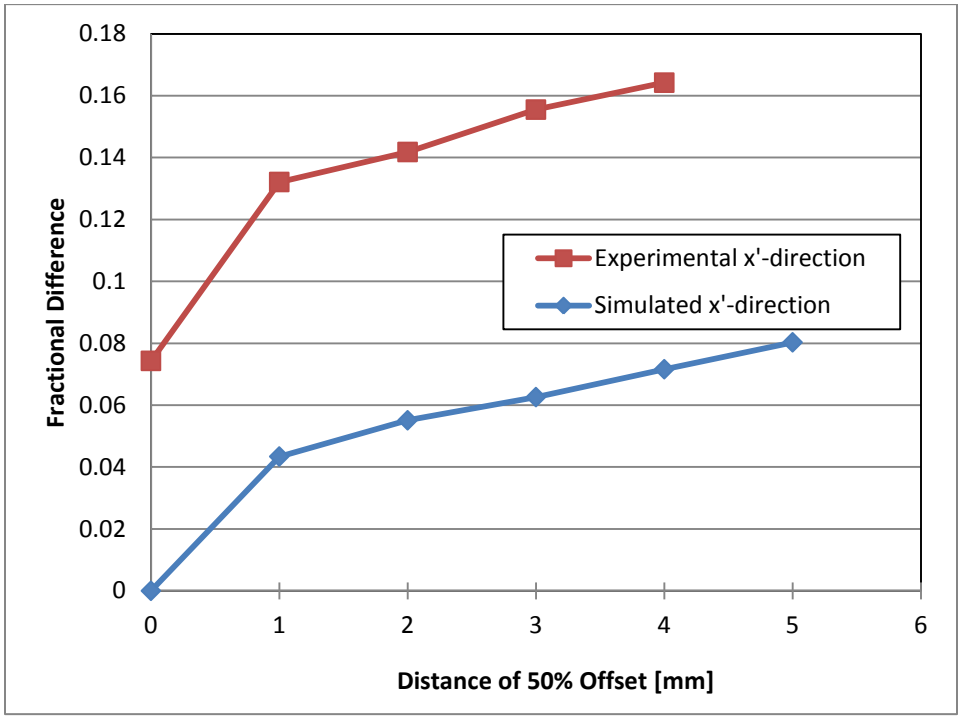

Figure 3-28. Fractional differences between motion-free and motion-corrected images with 50% of the scan taken at increasing offset distances of the phantom. The designation x' indicates that the motion was in the x-direction and occurred when the majority of this motion was along the s-axis.

The effect of the angle at which the offset occurred was studied by combining 50% of the sinogram for the object used at the relative starting position (i.e., 0 mm offset) with 50% of the sinogram for the object at offset distances of 1 mm - 4 mm (1 mm - 5 mm for the simulated data), but now varying the starting projection for the offset sinogram position. This simulates motions with respect to the s-axis direction, r-axis direction, or a

combination thereof. Figure 3-29 shows the results as fractional differences due to the angle at which the 50% offset motion started. The 4 mm offset data in Figure 3-28 correspond to the 180^{o} data for both experimental and simulated scans in Figure 3-29. We also show that the start offset angles between 0^{o} and 90^{o} have similar errors as those between 90^{o} and 180^{o}. The 90^{o} data correspond to the motion-correction shown in Figures 3-16 through 3-20. The r-axis motion produces better qualitative results and also lower quantitative errors.

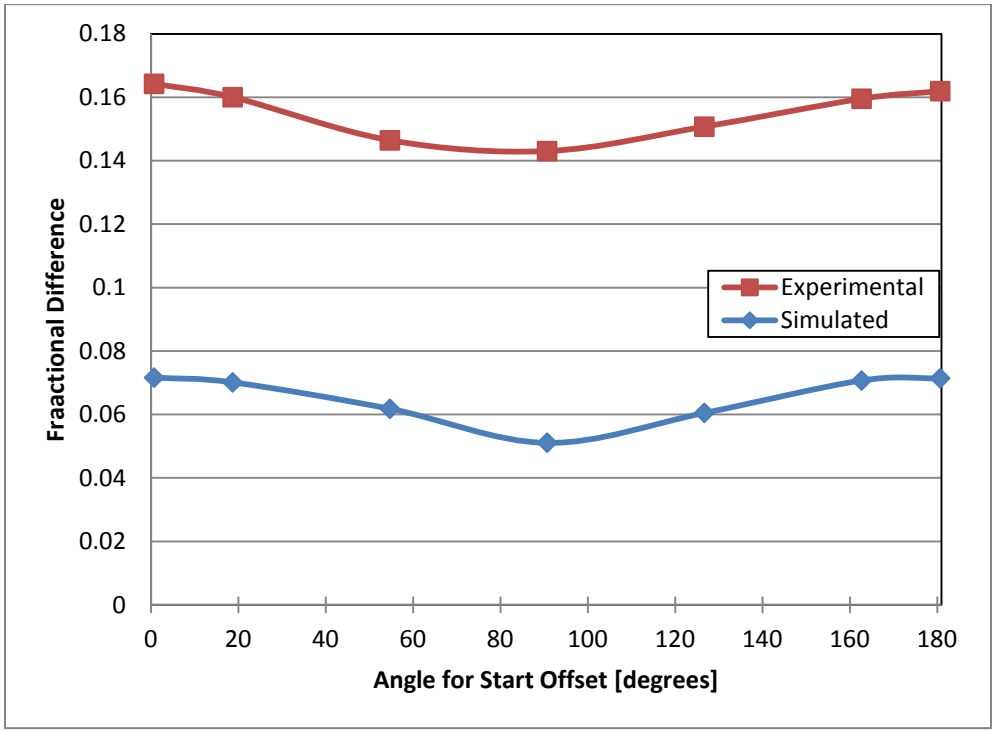

Figure 3-29. Fractional difference between motion-free and motion-corrected images with 50% of the scan taken at an offset distance of 4 mm of the phantom occurring at different times of the scanning process.

Finally, the effect of differing ratios of the scan of a moved object was produced by combining an increasing percentage of the sinogram for the object at an offset of 4 mm with the complementary percentage of the sinogram from the relative starting position (i.e., 0 mm offset). The increment of the 4 mm-offset sinogram ranged from 0 to 100% at 10% increments. The sinograms were reassembled consistently such that the motion

simulated always started primarily in the s-axis (i.e. x-axis motion at 180^{o}) and ended after the appropriate number of projections dependent on the ratio (e.g., 50 projections for 10%, 100 projections for 20%, etc.). Figure 3-30 shows the results as fractional differences due to increasing differing percentages of the 4 mm offset motion from the relative starting position. The 4 mm offset data from Figure 3-28 (and by extension the 180^{o} data from Figure 3-29) corresponds to the error for 50%.

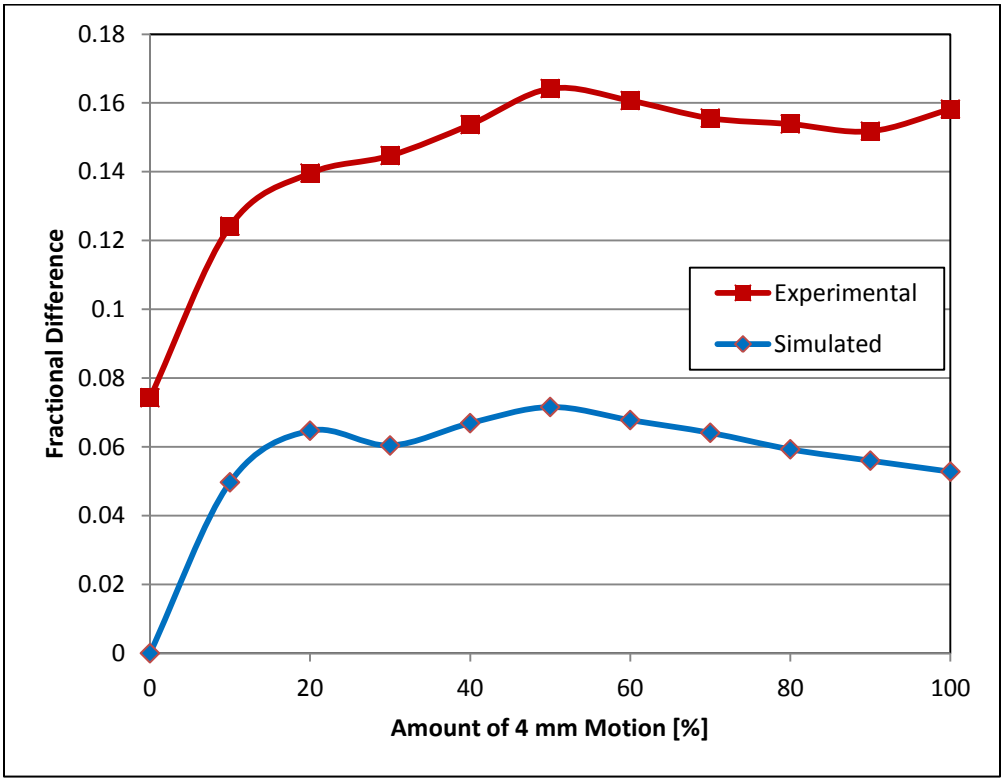

Figure 3-30. Fractional difference between motion-free and motion-corrected images with a 4 mm offset distance of the phantom for increasing amounts of motion-subjected times during the scan.

4. Conclusion

Several steps were taken to reduce the various artifacts that were present in the reconstructed image obtained from the fHRCT system. These artifacts could be broken into two categories: those due to system error and those due to subject motion. The artifacts due to the former were minimized by optimizing the scanner through geometric system parameter calculations and centering of the system, detector linearization, and beam hardening correction. The artifacts due to subject motion were minimized through the development of a motion-correction algorithm that reduced artifacts due to translational motion.

4.1 Scanner Optimization

The overall optimization of the scanner provided very good results. The initial parameters that were calculated were only slightly modified to improve the qualitative results of the image and provide a larger usable field of view. Some of the likely causes of these errors included, but were not limited to, incorrect assumptions for the position of the center row of the detector and the effects of mechanical and electrical noise within the system itself (seen in Figures 2-13 through 2-16).

The central row is the row of detector elements that represent the fan of the x-rays within the cone-beam, from which the projections can be reconstructed by a simple fan-beam reconstruction algorithm. Thus, if the assumptions for this row are incorrect or the

detector is not seated properly, so that the detector elements are not in the same plane defined by the rotational path of the source, the rest of the calculations for the scanner parameters will also be incorrect.

If detector element *E* is the central detector of the central row, the distance between the source and detector *E* is supposed to be the minimum compared to that of all detectors of the central row. Any error in the location of the detector *E* will increase the source-to-detector distance, and, consequently, the source-to-center and/or the center-to-detector distances calculated will also increase. To further complicate the calculations, the small mechanical and/or electrical imperfections in the system also caused small movements in the source-detector system, causing data detected by the detector elements to be incorrect. Therefore, the images were analyzed qualitatively as well, and a small change to the position of detector element *E* was applied to improve the images.

In general, success of the geometric parameter calculation process described is highly dependent on the accuracy of the calculation for the angle β_{normal}. Accuracy of this angle is mostly dependent on the angle increment between each projection. For the fHRCT system, even an error in β_{normal} as low as 0.0126 rad (0.72^{o}) can have a significant effect on the subsequent calculation for source position τ_o and location of detector element *E*. Thus, steps should be taken to achieve the greatest number of projections, even artificially through interpolation if necessary, so that the angle increment can be as small as possible.

The usable field of view was largely limited by the size of the gap between the detectors, making only one of the detectors useful for image reconstruction, as any object that

spanned across this gap would miss part of the projections. Therefore, only projection data from the detector on which the midline was incident were used to reconstruct the final image. The other detector was used only to determine N_{avg} and $N_{o,avg}$ (the means of the open field regions) to adjust for current fluctuations in the linearization process described in section 2.2.1.

The calibration of the detector through linearization was quite effective, demonstrated by the reduction of the ring artifacts. The use of the extra detector to adjust the open field data N_o based on $N_o' = N_o \times (N_{avg}/N_{o,avg})$ means that the open field data can be taken on a more intermittent basis (rather than before every scan) to maintain accuracy.

The beam hardening correction reduces, but does not eliminate, beam hardening artifacts. This is probably due to the type of beam hardening correction implemented, which utilizes a homogenous correction-calibration material, for correcting a heterogeneous phantom. Improvement of the beam hardening correction would include the use of a different type or additional filters to harden the beam before it interacts with the object and thus to minimize the effect of beam hardening [3]. Also, incorporating a material-selective beam hardening correction that utilizes the materials used in the phantom for a heterogeneous calibration material would further improve the resulting images [11].

4.2 Patient Motion Correction

The method of translational motion correction was determined to be sufficient for the maximum amount of subject motion that could occur and still remain within the field of view. This is approximately 11 mm for the 15.8 mm diameter phantom if placed near the edge of the 27 mm diameter field of view and moved to the exact opposite side of the

field of view. The errors were reduced, though not completely removed. However, by comparing the error after correction to the baseline established from Figure 3-26, the method performed very well for the small amounts of motion up to 4 mm (5 mm for the simulation). Even for the maximum fractional error of 0.1642 obtained for the experimental case (the peak error in Figures 3-28, 3-29, and 3-30), the value was not significantly different from the baseline error of 0.1599, with only a 2.7% increase. In many instances of the experimental case, the error is less than the baseline error. This can occur because the photon count deviation is a factor in the experimental case, and the motion-correction algorithm has a similar effect as that of a median filter on the projection data. Thus, when the amount of error due to photon variation is the more prominent error (i.e., when the amount of motion-correction is low), a lower error than the baseline value can result.

For motion offsets over 1 mm, the increase in error is directly proportional to an increase in motion distance that remained after the algorithm was implemented on the projections (Figure 3-28). The amount of error still present in the corrected images is also dependent on the direction of the motion (Figure 3-29), where motion along the r-axis creates less error than that along the s-axis. This means that the correction algorithm is more reliable in correcting for changes in magnification.

The accuracy of the algorithm also depends on the homogeneity of the uncorrected projections with each other, and, by consequence, the projections' overall proximity to the calculated ideal curves. For instance, when the projections from the phantom at two positions are involved in creating a motion-encoded sinogram, the motion-correction algorithm works best when profiles from one of the positions is more prevalent when

used in the calculation for ideal curves, rather than equal influence. Therefore it can be seen in Figure 3-30 that the greatest error occurs when the number of projections used to create the simulated motion are equivalent (i.e. 250 projections from the object at position A, 250 from the object at position B). These two positions equally affect the fit for the ideal curves, and the homogeneity between the positions (position A, B, and the ideal position calculated) is low.

Errors in correction were seen as streaks and blurring artifacts in the motion-corrected images. Several failures in the algorithm could explain these artifacts. Some of the most likely reasons for the artifacts include, but are not limited to, the following:

- Equidistant linear detectors produce unequal angles between adjacent rays. The larger the shift in the sinogram, the greater the error between the angles for the original rays and those for the new rays used for the reconstruction. In other words, an object at the center of the fan-beam is subjected to smaller magnification than an object at the periphery of the fan-beam.
- r-axis and s-axis motions are, for the most part, co-dependent for fan-beam equidistant-detector scanner systems. Only if the s-axis motion occurs when the centroid is along the fan-beam midline (i.e., the centroid position will not be shifted because of magnification) are they not co-dependent. Therefore, rarely will the projection data for the center of mass change without a change in the integral and vice versa. Practically, however, they cannot be simultaneously corrected in the sinogram space.
- The center of mass curve is not as accurate as the integral curve. Since the center of mass does not create the ideal sinusoid that the integral curve does, an

adjustment must be made from the Fourier sinusoid fit to a sinusoid-like curve fit using Equation 2.1. This means that the centroid location (x_o, y_o) must be estimated before an ideal fit can be calculated. Errors occur because the fit requires an estimate for the centroid location (x_o, y_o) based on the polar-to-Cartesian conversion of r and φ obtained after the Fourier sinusoid fit and magnification adjustment. Due to the geometric properties of the fan-beam, the value of r tends to be slightly overestimated, and the angle φ may be either over- or underestimated. This is the primary cause of error in the fit, and the estimate of (x_o, y_o) increases in error as the actual distance of the centroid from the center-of-rotation increases. This leads to a less accurate fit than the one acquired for the integral, though this method creates a better fit than a simple sinusoid fit.

Future work of the motion-correction algorithm will involve attempting to fix the above issues. The method proposed for correcting motion can only realistically be improved by modifying the reconstruction algorithm, as further development for corrections made in the sinogram space are limited. Modifying the reconstruction algorithm could also lead to simultaneous correction of errors in the r-axis and s-axis direction. Lastly, improvement of the calculation for the ideal center of mass curve will be considered by further utilizing Equation 2.1 to determine the centroid location (x_o, y_o) by the chi-square reduction of this equation after the system parameters are already calculated.

Both the parameter-calculation and motion-correction algorithms can be further improved for transition from 2D fan-beam image reconstruction to 3D cone-beam image reconstruction. For the fHRCT parameter calculation, a method to find the optimal center along the z-axis must also be developed and implemented. In a similar fashion, the

method for motion correction must be improved to account for the addition of a potential z-axis motion. This means additional calculations must be made to determine the sum of intensities and the center of mass location in a 2D space (as opposed to a 1D space) for each projection.

5. References

[1] G. T. Gullberg, B. M. Tsui, R. C. Crawford and R. E. Edgerton, "Estimation of geometrical parameters for fan beam tomography," *Physics in Medicine and Biology, 32,* pp. 1581-1594, 1987.

[2] J. Sibjers and A. Postnov, "Reduction of Ring Artefacts in High-Resolution Micro-CT Reconstructions," *Physics in Medicine and Biology*, 49, pp. N247-N253, 2004.

[3] J. F. Barrett and N. Keat, "Artifacts in CT: Recognition and Avoidance," *RadioGraphics, 24,* pp. 1679-1691, 2004.

[4] J. Jakubek, "Data Processing and Image reconstruction Methods for Pixel Detectors," *Nuclear Instruments and Methods in Physics Research Section A: Accelerators, Spectrometers, Detectors and Associated Equipment*, 576, pp. 223-234, 2007.

[5] A. C. Kak and M. Slaney, Principles of Computed Tomography, New York: The Institute of Electrical and Electronics Engineers, Inc., 1988.

[6] G. T. Gullberg, C. R. Crawford and B. M. W. Tsui, "Reconstruction Algorithm for Fan Beam with a Displaced Center-of-Rotation," *IEEE Transactions on Medical*

Imaging, 5, pp. 23-29, 1986.

[7] W. Mao, T. Li, N. Wink and L. Xing, "CT Image Registration in Sinogram Space," *Medical Physics*, 34, pp. 3956-3602, 2007.

[8] W. Lu and T. R. Mackie, "Tomographic Motion Detection and Correction Directly in Sinogram Space," *Physics in Medicine and Biology*, 47, pp. 1267-1284, 2002.

[9] Z. Mu, D. Fu and G. Kuduvalli, "A Probabilistic Framework Based on Hidden Markov Model for Fiducial Identification in Image-Guided Radiation Treatments," *IEEE Transactions on Medical Imaging*, 27, pp. 1288-1300, 2008.

[10] J. A. Concepcion, J. D. Carpinelli, G. Kuo-Petravic and S. Reisman, "CT Fan Beam Reconstruction with a Nonstationary Axis of Rotation," *IEEE Transactions on Medical Imaging*, 11, pp. 111-116, 1992.

[11] P. Rüesegger, T. Hangartner, U. Keller and T. Hinderling, "Standardization of Computed Tomography Images by Means of a Material-Selective Beam Hardening Correction," *Journal of Computed Assisted Tomography*, 2, pp. 184-188, 1978.